Characterization and Application of Nanomaterials 2025, 8(2), 10951.
https://doi.org/10.24294/can10951

Article

SERS characterization of Rhodamine 6G dye molecule response using thin gold film covalently immobilized with gold nanourchins

Mohammad E. Khosroshahi[1,2,3,*], Yesha Patel[1,4], Christine Gaoiran[1], Vithurshan Umashanker[1,5]

[1] Nanobiophotonics & Biomedical Research Laboratory, M.I.S. Electronics Inc., Richmond Hill ON L4B 1B4, Canada
[2] Institute for Advanced Non-Destructive and Non-Invasive Diagnostic Technologies (IANDIT), University of Toronto, Toronto ON M5S 3G8, Canada
[3] Department of Mechanical and Industrial Engineering, University of Toronto, Toronto ON M5S 3G8, Canada
[4] Department of Biochemical Engineering, University of Waterloo, Waterloo ON N2L 3G1, Canada
[5] Department of Electrical and Computer Engineering, University of Waterloo, Waterloo ON N2L 3G1, Canada
*** Corresponding author:** Mohammad E. Khosroshahi, m.khosro@miselectronics.com, me.khosroshahi@gmail.com

CITATION

Khosroshahi ME, Patel Y, Gaoiran C, Umashanker V. SERS characterization of Rhodamine 6G dye molecule response using thin gold film covalently immobilized with gold nanourchins. Characterization and Application of Nanomaterials. 2025; 8(2): 10951. https://doi.org/10.24294/can10951

ARTICLE INFO

Received: 17 December 2024
Accepted: 28 February 2025
Available online: 3 April 2025

Abstract: We report on the measurement of the response of Rhodamine 6G (R6G) dye to enhanced local surface plasmon resonance (LSPR) using a plasmonic-active nanostructured thin gold film (PANTF) sensor. This sensor features an active area of approximately ≈ 2.5 × 10^{13} nm^2 and is immobilized with gold nanourchins (GNU) on a thin gold film substrate (TGFS). The hexane-functionalized TGFS was immobilized with a 90 nm diameter GNU via the strong sulfhydryl group (SH) thiol bond and excited by a 637 nm Raman probe. To collect both Raman and SERS spectra, 10 µL of R6G was used at concentrations of 1 µM (6 × 10^{12} molecules) and 10 mM (600 × 10^{14} molecules), respectively. FT-NIR showed a higher reflectivity of PANTF than TGFS. SERS was performed three times at three different laser powers for TGFS and PANTF with R6G. Two PANTF substrates were prepared at different GNU incubation times of 10 and 60 min for the purpose of comparison. The code for processing the data was written in Python. The data was filtered using the *filtfilt* filter from *scipy.signals*, and baseline corrected using the Improved Asymmetric Least Squares (ISALS) function from the *pybaselines.Whittaker* library. The results were then normalized using the *minmax_scale* function from *sklearn.preprocessing*. Atomic force microscopy (AFM) was used to capture the topography of the substrates. Signals exhibited a stochastic fluctuation in intensity and shape. An average corresponding enhancement factor (EF) of 0.3 × 10^5 and 0.14 × 10^5 was determined for PANTF incubated at 10 and 60 min, respectively.

Keywords: thin film; gold nanourchins; R6G molecule; SERS; FT-NIR; enhancement factor

1. Introduction

There has been a great interest in recent years in the potential applications of nanostructured materials in analytical chemistry, molecular biology, and biochemical analysis [1–3]. In contrast to Rayleigh scattering, Raman scattering is an inelastic process where photons undergo scattering, and the energy of molecular transitions is detected by measuring the change in wavelength or frequency shift of the scattered photons, typically analyzed using Raman spectroscopy (RS). As a result, a chemical fingerprint of the sample is achieved for identification and quantitation. To be Raman-active, the molecular vibrations induced by an external electric field, such as a laser, should be able to induce a change in the polarizability of molecules within the sample, which gives rise to Raman scattering. The intensity of scattered light varies with the change in the molecular polarization. Raman shift is an intrinsic property of a molecule. By measuring the intensity of the scattered light as a function of frequency

shift in cm^{-1}, one can obtain insights into molecular vibration. Thus, it makes RS a powerful label-free and non-destructive analytical tool to distinguish biological constituents and conformation through their molecular vibrational modes. Unfortunately, in the spontaneous Raman, the Stokes and anti-Stokes scattering are so weak and inefficient that only about 1 in 10^7 photons can be detected, with a cross-section of $\approx 10^{-30}$ cm^{-2}. However, the efficiency can be improved using surface-enhanced Raman scattering (SERS), which is an ultrasensitive, non-destructive optical technique that has been utilized for biosensing of analytes at very low concentrations in solutions or deposited as a monolayer on nanostructured metal substrates [4–7]. There has been increasing interest in developing advanced SERS-based non-invasive point-of-care devices for clinical applications, particularly in the early diagnosis of cancer. This is because the advances in ultrasensitive instrumentation for SERS and nanostructure-enhanced SERS studies provide more accurate detection and identification of the analyte and vibrational spectrum of high information content for molecules in room-temperature colloids [1,8–11] and solid surfaces [12–16].

Plasmonics is the study of how light interacts with charged particles, particularly electrons in metals. It primarily involves the excitation of electromagnetic modes when these particles are influenced by an external electric field E_0, leading to a collective oscillation of the conduction band electrons within the metal. In the case of thin metal film, the electronic charge density is delocalized called surface plasmon polaritons (SPP), which are confined near the metal-dielectric interface, propagating over relatively large distance, for example, about 5–10 μm for gold. However, in the case of NPs with subwavelength sizes, the oscillations are localized, called localized surface plasmon (LSP). Gold, as a noble and the most non-reactive of all metals, has excellent corrosion resistance in moist air, resistance to oxidation, and catalytic characteristics, and is widely used in optical sensor applications. The optical properties of plasmonic nanoparticles (PNPs) offer significant advantages, including considerable optical attenuation due to absorption and scattering associated with localized surface plasmon resonance (LSPR) [17,18], nonlinear optical properties, surface-enhanced scattering, tunable resonance in the visible-NIR range, low oxidation, time-dependent absorption, and biocompatibility. These properties are determined by nanoparticle size, shape, refractive index, and density of the surrounding environment [19–23].

Normally, SERS can be accounted for by two main mechanisms: (a) LSPR-induced electromagnetic (EM) field enhancement at the molecular positions due to coupling of enhanced local electric field $E(\omega_l)$ at frequency ω at the surface of the PNP caused by the induced dipole of plasmon oscillation to the incident field E_0. The enhancement depends on the topology of the metallic film, the size and shape of the NPs, and the strong light absorption and scattering that occur at the SPR frequency; and (b) charge transfer (CT), i.e., a molecular chemisorption during which the electrons are transferred from the analyte molecules into the vacant levels on the metal surface. As a result, a new band forms in the electronic spectrum of the molecule due to the electronic excitation of the coupled molecule-metal surface. It is noteworthy that CT is limited to molecules adsorbed directly on the metal surface, whereas EM effects can act as a nanoantenna to transfer the SPR radiation over a certain distance from the

origin. The enhancement is usually expressed as$|E(\omega_l)|^4/|E_0|^4$, but in more precise evaluations, the dipole reradiation term $E(\omega_{re})$ specifically the Raman emitted frequency is also included $|E(\omega_l)|^2|E(\omega_{re})|^2/|E_0|^4$ [24]. The resonant frequency of a PNP is dependent on its size, shape, material properties, and surrounding medium [15–24].

The SERS intensity depends on several factors, including a) the type of substrate, as they react differently to SERS; b) the type, shape, and the size of nanostructure as each plays a key role and responds differently; c) the type of analyte, as various molecules have different Raman scattering, i.e., the greater the cross-section, the more intense the Raman scattering; and d) an optical setup with a higher numerical aperture objective improves Raman collection efficiency.

Uniformly distributed and self-assembled PNPs can enhance Raman scattering when introduced into a sample by increasing the number of hot spots or nanogaps, which effectively amplifies the electric field, leading to enhanced Raman signal. Among the various nanostructures with different geometrical shapes, GNU is an anisotropic three-dimensional nanocrystal that possesses unique optical properties compared to spherical gold nanoparticles of the same core diameter. This distinction arises from its uneven, spiky surface, which causes a redshift in the SPR peak and creates a greater enhancement of the $E(\omega_l)$ at the tips of the GNU. This enhancement is confined to a smaller and more localized area [25]. The larger aspect ratio of the branches and plasmon hybridization between the spike core and tips enhances the polarization sensitivity of GNU by inducing different dipole moments [26,27]. GNU enhances the electric field due to hot spots, high core-tip aspect ratio, and off-resonant excitation at 637 nm of the Raman probe compared to the plasmon absorption band of 90 nm GNU at 652 nm.

Previously, we reported the SERS detection of cancer biomarkers using a thin gold film substrate [28] where the planar nanometer-thin film was used as a two-dimensional plasmonic-active nanostructure; however, it was not considered as PANTF, i.e., a nanostructure possessing the properties of both thin films and individual nanoparticles. The importance of PANTF is due to reproducible hotspots between thin film-PNS and its rich plasmonic properties caused by the hybridization between the LSPR of NPs and propagating surface plasmon polaritons (SPP) of the metallic film. The physicochemical properties, including electrical, thermal, mechanical, and optical properties, of thin films can be significantly influenced by the roughness of the substrate. Recent studies have examined the optical properties of noble-metal NPs in proximity to a metal film [29,30]. These studies have demonstrated that the localization and field strength in the plasmonic gap are significantly influenced by factors such as nanoparticle composition, the film characteristics, nanoparticle size and shape, and the distance of the plasmonic gap [29,31].

Therefore, choosing rough metallic substrates plays a key role in achieving SERS since the enhancement is heavily influenced by the shape, size, morphology, distribution of NPs, and EF of the substrate [32–40]. The goals of the present work are to a) fabricate GNU-based PANTF; and b) characterize and compare the interaction of the R6G dye with TGFS and PANTF using FT-NIR and SERS. The goal of this ongoing research is to develop a multiplexed PANTF-based nanobiosensor for the active detection of cancer biomarkers in serum.

2. Materials and methods

For assembly of the GNU-gold film substrate, deionized (DI) water (6442-85), reagent alcohol (277649), 1,6-hexanedithiol (H12005), ultrapure water (6B7133), and 95% Rhodamine 6G (R4127) were purchased from Sigma-Aldrich. 70% ethanol (BP820) was purchased from Thermo Fisher. Citric acid-stabilized GNU with a 90 nm diameter and 8.92×10^{-12} molar concentration was purchased from Cytodiagnostics (GU-90-20). Phosphate buffered saline, pH 7.4 (10010031), was purchased from Gibco. Commercially available sealed gold thin film substrates (SPR-1000-050) with 10 nm gold thickness prepared by conventional electron beam evaporation were purchased from Platypus Technologies. Low retention 1.5 mL microcentrifuge tubes (3451PK, Biolynx) were used as reaction tubes. Equipment used in the reaction process was a microcentrifuge (OF-17710-11), a centrifugal filter (UFC503096, Millipore Sigma), an ultrasonic bath (Elmasonic), an orbital shaker (RK-51700-13), and a vortex shaker (RK-04729-07) purchased from Cole-Palmer, Canada; a combo pH meter (BLU2300E, Canada), an analytical balance (Sartorius, USA); as well as micropipettes and micropipette tips (Eppendorf, 2231302001).

For the investigation of the enhancement factor using R6G as a probe molecule, a Raman concentration of 10 mM and an SERS concentration of 1 μM were used. The SERS concentration accounts for the increased surface area as a result of the GNU presence on the substrate [41–43]. For each Raman and SERS reading, 10 μL of the respective R6G concentration was added to the substrate. Spectra were collected at 637 nm at varying laser powers (2, 4, and 8 mW).

3. Substrate preparation

The preparation procedure of the GNU-immobilized TGFS for the SERS experiment is schematically shown in **Figure 1**.

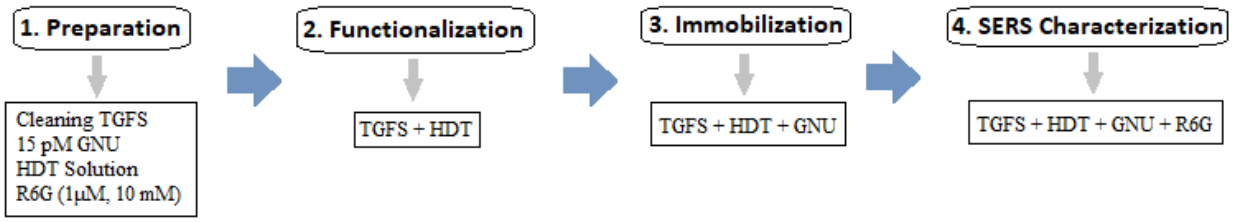

Figure 1. Schematic representation of GNU-immobilized TGFS.

3.1. Cleaning of gold substrate

A previously cut 1 × 1 cm piece of the TGFS was placed in its own respective plastic circular container as a functionalization chamber. A total of 500 μL of 70% ethanol was added to the container to completely submerge the substrates. The container was sealed and sonicated at 60 kHz and 60% power for 10 min. The substrate was rinsed twice with fresh ethanol to remove any remaining debris. The substrate was left to air dry and stored in an airtight container until further use.

3.2. Preparation of 15 pM concentrated GNU

In a Class II A2 biosafety cabinet (LabGard, USA), 1.12 mL, 1.12 mL, and 1.13 mL of 90 nm GNU were added to three separate microcentrifuge tubes. To maintain balance, 1.13 mL of water was added to a fourth tube. The tubes were then placed in a microcentrifuge and spun at 3200 rpm for 30 min. After centrifugation, the supernatant was discarded, leaving 25 μL of GNU pellet in each tube. The GNU pellets were then resuspended by adding 560 μL of ultrapure water to the tube that contained 1.12 mL of GNU and 565 μL of ultrapure water to the tube containing 1.13 mL of GNU. The three resuspended GNU solutions were combined in a 20 mL scintillation vial, resulting in a total volume of 1.685 mL resuspended GNU. To achieve a final volume of 2.013 mL at a concentration of 15 pM, 350 μL of ultrapure water was added to this vial.

3.3. Preparation of ethanolic hexane (HDT) solution

The concentrated GNU was immobilized on a TGFS via gold-thiol bonds. In the biosafety cabinet, 1999 μL of pure ethanol reagent alcohol was mixed with 1 μL of 1,6-hexanedithiol in a 20 mL glass scintillation vial, which was then immediately capped. The vial was vortexed at 1800 rpm to prepare a 2 mL solution of 3 mM HDT.

3.4. Preparation of 10 mM R6G

9.60 mg of R6G dye was accurately weighed using an analytical balance and then added to a scintillation vial containing 2 mL of ultrapure water. The solution was vortexed at 1800 rpm to create a 10 mM R6G stock solution.

3.5. Preparation of 1 μM R6G

0.5 μL of the prepared 10 mM R6G stock solution was added to a scintillation vial containing 4999.5 μL of ultrapure water. The resulting mixture was vortexed until homogeneous to obtain 5 mL of 1 μM R6G solution.

3.6. Functionalization of TGFS with HDT and GNU

The cleaned gold chip was immersed in a vial containing 2 mL of 3 mM HDT and then sonicated at 60 kHz and 60% power for 2 min to functionalize the TGFS with HDT molecules. After sonication, the substrate was rinsed twice with 70% ethanol followed by ultrapure water to remove any unbound HDT molecules. Immediately following the rinsing, 200 μL of prepared 15 pM GNU was pipetted onto the gold surface. The container was sealed and placed on the orbital shaker for 10 min at 150 rpm to allow GNU to bind to the free thiol end of HDT. The substrate was rinsed then with ultrapure water and air-dried in the biosafety cabinet before characterization using Raman spectroscopy.

4. Characterization

10 μL each of 10 mM and 1 μM R6G samples were pipetted separately onto the GNU-functionalized substrate. The substrate was analyzed using Raman spectroscopy as outlined in this section. The remaining volumes of 10 mM and 1 μM R6G samples were transferred to their respective cuvettes. These solutions were analyzed using UV-

Vis, fluorescence, FT-NIR, and Raman spectroscopy as described. The absorbance of the two R6G solutions was measured using the Jenway 7205 UV-Vis spectrometer with a wavelength range of 200–800 nm (Cole-Palmer). Fluorescence spectra of the identical solutions were recorded using a 532 nm laser with a power output of 50 mW. The fluorescence emission was transmitted by a 500 μm core diameter optical fiber to the FLAME-T-XR1-ES spectrometer (Ocean Optics). The spectrometer was equipped with a 2048-pixel (14 μm × 200 μm) linear silicon CCD array. The device had a detection range spanning from 200 nm to 1050 nm and an optical resolution of 1.5 nm full-width half maximum (FWHM). FT-NIR spectra were recorded using a tungsten halogen light source, with a wavelength range between 360 and 2500 nm, and an output power of 8.8 mW. The light was transmitted through a 400 μm core diameter optical fiber (NANOQ-FIBER-400-VIS-NIR) and detected by the NanoQuest 2.5 spectrometer (Ocean Insight) with the transmission scan time being 5 s with an 8 nm resolution.

The SERS spectra were obtained using a benchtop 637 nm laser with a tunable output power of up to 10 mW (S1FC637, Thorlabs, USA) connected to a 638 nm Raman probe (RIP-RPB-638-FC-APC-SMA, Ocean Insight, USA). The Raman parameters on the OceanView software were set to an integration time of 5 s, a number of scans of 3 to average, and a boxcar width of 5. Nonlinearity correction and clean peaks options were applied, and a background spectrum was acquired with the Raman probe shutter closed. The Raman probe contains a fiber bundle, which directs excitation light from the laser to the sample and collects the Raman scattered light within a spectral range between 300–3900 cm^{-1}. The working distance of the probe was 1.8 cm perpendicular to the substrate, creating a 3 mm laser diameter comparable to the sample drop size. The beam was centered in the middle of the droplet without directly interacting with the surface of the substrate before SERS spectrum was obtained. The experiment was performed using the laser at 2, 4, and 8 mW, respectively. While conducting measurements, the light at the laser's wavelength (known as Rayleigh scattering) was blocked along the path to the spectrometer (HDX-Vis-NIR, Ocean Insight, USA) using a dichroic filter that has a spectral sensitivity range of 150–3400 cm^{-1} to avoid saturating the detector.

5. Results and discussion

The absorbance of 90 nm GNUs is shown in **Figure 2** with a bandwidth between 500 and 800 nm and a single broad LSPR peak at about 652 nm. The inset shows the morphology of a single GNU with short and long branches, which play a key role in the field enhancement.

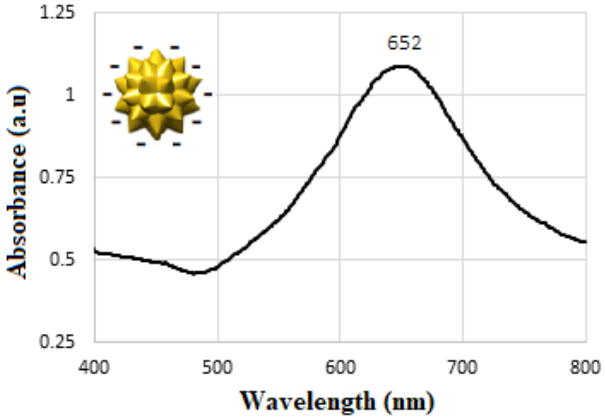

Figure 2. UV-Vis absorbance of GNU with a maximum SPR peak at 652 nm.

Figure 3a illustrates a scanning electron microscope (SEM) image of a single, multi-branched GNU morphology with each tip having an axial size of ≈ 12 nm. An example of clustered GNU is shown in **Figure 3b**, where it causes an increase in size and the height of the nanostructure, which in turn red-shifts the SPR. The coupling between clusters of metal NPs becomes important and can influence the SERS results. The clustering or aggregation of NPs increases with the incubation time. Unlike the densely packed single GNU layer in a 2-D plane, clusters tend to form at the top layer and in overlapping areas due to the spatial overlap of double-layer clusters. The randomly distributed nanogaps between the individual GNUs or aggregates can excite the gap plasmon modes [44]. The larger GNUs exhibit a LSPR peak at longer wavelengths because the branches facilitate more extended longitudinal plasmon resonance [45]. A two-dimensional AFM image of a single GNU is shown in **Figure 3c**. In our study, we maintain a constant diameter for the GNUs (neglecting the clustering); the ratio of center-to-center distance (D) between GNUs to the radius R_p of the GNU (D/R_p) decreases as (D) decreases or the particle size increases. As a result, we anticipate a stronger plasmon resonance coupling, which could lead to a greater positive shift in the LSPR wavelength when the interparticle distance decreases.

Previous work suggests that the coupling, hence the resonance shift, becomes negligible at $D \geq 2.5$ times the nanoparticle size [46]. In addition, since most of the GNUs are well separated with a narrow size range of 80–90 nm in diameter, it indicates a strong correlation between the particle size and enhancement efficiency.

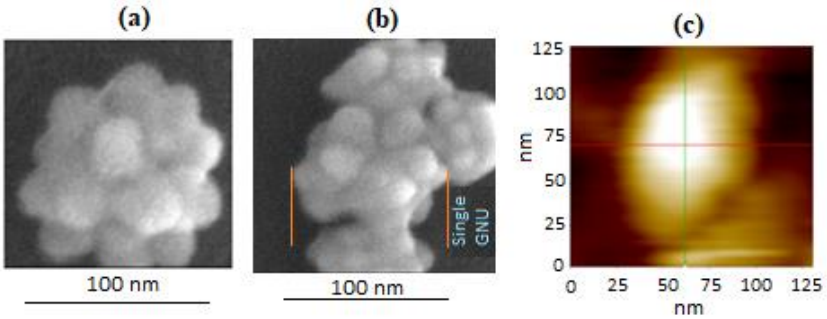

Figure 3. SEM of **(a)** single GNU showing the branched surface topology, **(b)** clustered GNUs, and **(c)** 2D AFM of GNU.

Prior to the experiments of R6G interaction with the substrate, UV-Vis, fluorescence spectroscopy, and the Raman scattering of pure R6G molecules in solution were performed at 1 μM and 10 mM. R6G is a cationic dye, and the molecule contains 12 aromatic bonds, 5 double bonds, 36 non-H bonds, 17 multiple bonds, and 7 rotatable bonds, 4 six-membered rings, i.e., benzene, which has 6 carbons, 2 ten-membered rings, 1 aromatic ester, 1 aliphatic imine, 1 aromatic secondary amine, and 1 aromatic ether. To avoid saturation during UV-Vis spectroscopy at 10 mM, 9 μL of R6G stock solution was diluted in a cuvette containing 2991 μL ultrapure water to obtain 0.03 mM R6G. **Figure 4a** illustrates the molecular structure of R6G with the corresponding UV-Vis spectrum of 1 μL of R6G in ultrapure water shown in **Figure 4b** with a main peak at around 530 nm relating to a transition moment due to $\pi*$-π transition, and less intense peaks at 257 and 350 nm, respectively, corresponding to transitions to higher singlet excited states. Since there is a linear dependence between the initial concentration of R6G at their maximum absorption, at the higher concentration of 0.03 mM, the main peak at 530 nm and the secondary peaks become stronger (**Figure 4c**). Solvent molecules can interact with the molecules of absorbing species of ground or excited state(s) through intermolecular bonding, resulting in a change in the wavelength of absorption due to a decrease or increase in the energies of the ground or excited states. It is noteworthy that the position of the band may vary with solvent, which is usually attributed to solvent parameters such as polarity and refractive index; however, the intensity or the amplitude of response, i.e., the population of excited molecules, is directly related to laser intensity as well as the concentration and path length.

The fluorescence emission spectrum of R6G is shown in **Figure 5a** with a maximum peak at 571 nm. **Figure 5b** indicates the comparison of fluorescence emission of two different concentrations at 1 μM and 0.03 mM, where the higher concentration exhibits a higher emission intensity. The samples prepared at 1 μM, 0.03 mM, and 10 mM are shown in **Figure 5c–e**, with the corresponding images of fluorescence emission illustrated in **Figure 5f–h**, respectively.

It is noted that as expected at higher concentrations, the emission becomes stronger, but at 10 mM no result was obtained due to total optical attenuation. The brightness of the fluorescence emission is defined as $B = Q_y/\varepsilon$, where $Q_y = \frac{k_r}{k_r+k_{n_r}}$, k_{n_r} and k_r are non-radiative and radiative decay rates, respectively, and the molar absorption coefficient ε (M^{-1} cm^{-1}) is directly proportional to quantum yield. Using the Beer's law in a dilute solution, the intensity of measured fluorescence emission is given by $I_f = Q_y P_0(1 - 10^{-\varepsilon cl}) \approx Q_y P_0 \varepsilon cl$ where P_0 is the laser power, c is the concentration of analyte, and l is the optical path length, respectively, i.e., the higher the value of B, the higher it will be I_f.

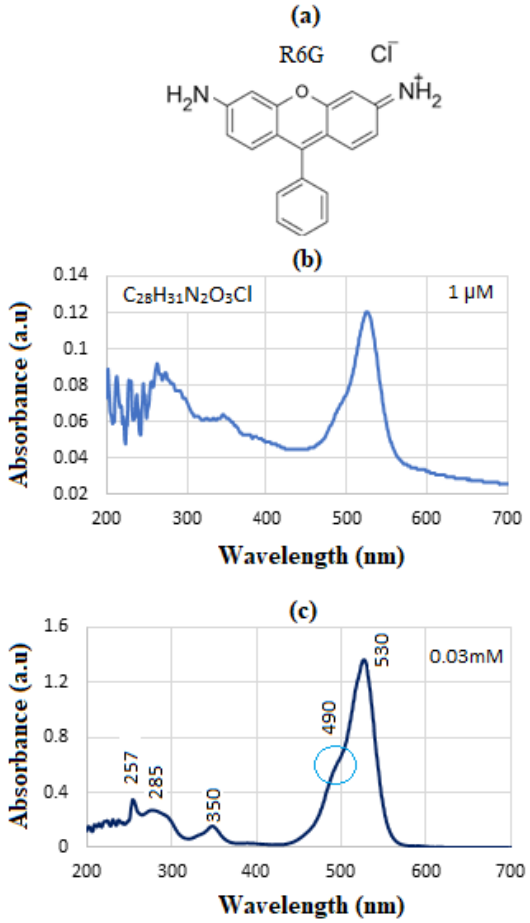

Figure 4. (a) Molecular structure and UV-Vis spectra of R6G at **(b)** 1 µL and at **(c)** 0.03 mM.

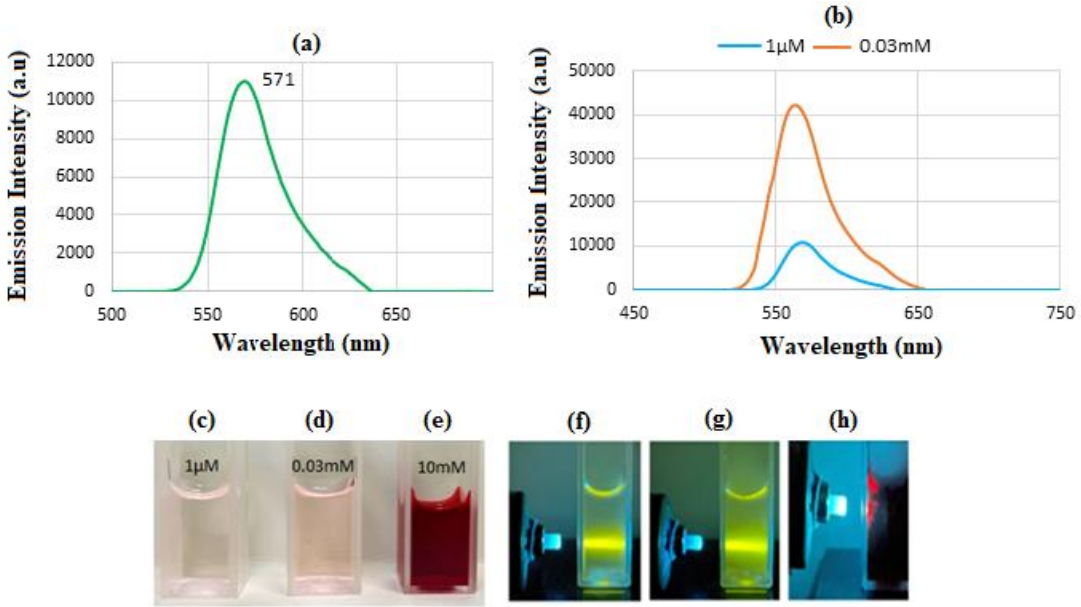

Figure 5. (a) Fluorescence emission of R6G at 571 nm excited by 532 nm laser, images of the sample prepared at different concentrations of **(b)** 1 µM, **(c)** 0.03 mM, and **(d)** 10 mM with corresponding fluorescence emission shown in **(e)**, **(f)**, and **(g)** respectively, and **(h)** shows the corresponding fluorescence emission of 1 µM and 0.03 mM, respectively.

Figure 6 illustrates the Raman spectra of dilute R6G solution at various concentrations of 0.03 mM and 10 mM, where each result is the average of three trials. The intensity of the lines in the case of 10 mM is higher than those at 0.03 mM, and two peaks at 1386 and 2757 cm^{-1} corresponding to aromatic C-C and ester(s) stretching modes are closely overlapped. Previous work has reported that the intensity of active modes is sensitive to the π-electron configuration of R6G located at the nitrogen atoms of the ethylamine external groups through the xanthene ring [47]. The amount of scattered light is directly proportional to the product of the weight-average molar mass, the solute concentration, and the polarizability of the molecule. The polarizability, in turn, is influenced by the molecular size and weight. Therefore, larger particle polarizability results in a greater magnitude of induced polarization and higher signal intensity.

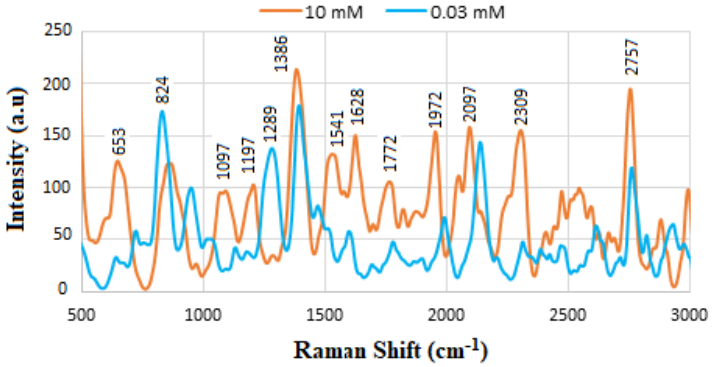

Figure 6. Averaged Raman spectrum for pure R6G using 0.03- and 10-mM solutions.

The Raman spectra are superimposed for comparison. The peak at 653 cm^{-1} corresponds to C-C ring in-plane bending, 824 and 1097 cm^{-1} are related to C-H out-of-plane bending, and the peak at 1289 cm^{-1} likely corresponds to N-H in-plane bend mode. Most significant peaks between 1300 and 1700 cm^{-1} indicate aromatic esters. Therefore, the overlapped peaks probably correspond to aromatic C-C and N-H stretching modes. This can be due to over-masking at the higher concentration. In addition, the Raman lines at higher concentrations between 500 and 1500 cm^{-1} are blue-shifted compared to the lower concentration. The most dominant lines start from the bottom of **Table 1,** moving upwards in the order of decreasing intensity, i.e., the highest lines belong to N-H stretching modes and the least to C-C ring in-plane bending in Xanthene/phenyl. The corresponding Raman lines are shown in **Table 1** [47–52].

Figure 7a shows an example of TGFS prior to adding R6G. The optical picture of the TGFS is shown in **Figure 7b** and the 2-D AFM images of the initial substrate as supplied are shown in **Figure 7c,d**, respectively, before and after magnification. **Figure 7e** indicates an enlarged portion of **Figure 7d** with the corresponding histogram of the surface. The 3-D image is shown in **Figure 7f**, where the surface appears to have some micro-level size scratches, irregularities, and impurities shown as bright spikes despite our initial thorough cleaning of the substrate with ethanol prior to imaging.

Table 1. Assignments corresponding to the Raman shifts observed for pure R6G [47–52].

Raman Shift (cm^{-1})	Assignment	Reference
613	C-C-C ring in-plane vibration mode	[45]
772	C-H out-of-plane bend mode	
1126, 1185	C-H in-plane bend mode	
1312, 1575	N-H in-plane bend modes	
1362, 1510, 1648	C-C stretching modes	
780	Aromatic C-H bending mode	[46]
1199	C-O-C stretching mode	
1375, 1511, 1545, 1580, 1650	C-C stretching mode	
772, 1187	C-H out-of-plane bending vibration	[47]
1313, 1366, 1513, 1652	Aromatic C-C stretching	
608	in-plane bending vibration	[48]
772	C-H out-of-plane bending vibration	
1184, 1309, 1362, 1495, 1567, 1646	In-plane C-C stretching vibrations	
614	C-C-C ring	[49]
779	out-of-plane bending of C-H	
1183	C-H stretching	
1312	in-plane bending of C-O-C	
1364, 1511, 1576, 1652	C-C stretching of the aromatic ring	[50]
612	C-C ring in-plane bending in xanthene/phenyl ring	
772	C-H out-of-plane bending	
797	Hybrid mode xanthene/phenyl rings	
1127	C-H in-plane bending in xanthene/phenyl rings	
1187	C-H in-plane bending in xanthene ring	
1204	Hybrid mode (xanthene/phenyl rings)	
1275	C-O-C stretching $COOC_2H_5$ group on phenyl ring	
1312	Hybrid mode (xanthene/phenyl rings & NHC_2H_5 group)	
1363	C-C stretching in xanthene ring	
1449	C-N stretching NHC_2H_5	
1509	C-C stretching in xanthene ring	
1575	C-C stretching in phenyl ring	
	Hybrid mode (phenyl ring with $COOC_2H_5$	
1651	C-C stretching in xanthene ring	
1700–2800	Ester(s) aromatic	
> 2800	NH stretching modes	

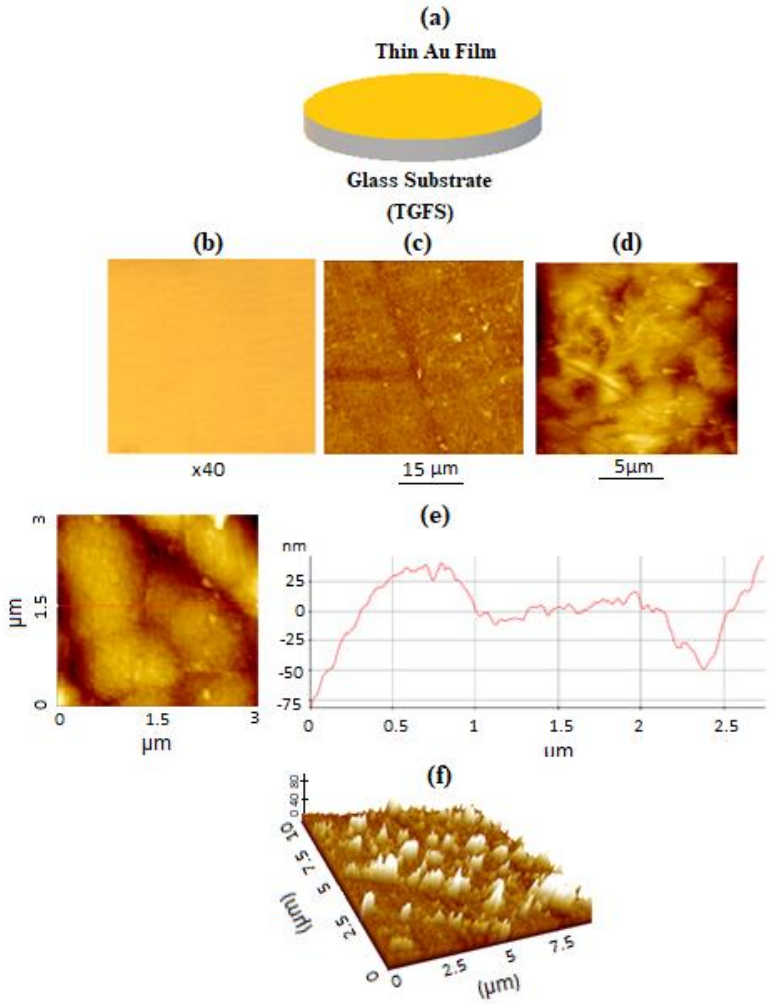

Figure 7. (a) Schematic diagram of TGFS; **(b)** optical and 2D AFM images of TGFS; **(c)** before; **(d)** after magnification; **(e)** enlarged portion of **(d)** with the corresponding histogram; and **(f)** 3D image showing some rough morphology.

In diffuse reflectance measurement, a reference reflector such as gold acts as a reference for background measurement and exhibits extremely high reflectance in the NIR region. The corresponding FT-NIR reflectivity of TGFS in **Figure 8a** shows the dominant strong signals in the 4500–5200 cm^{-1} (2.2–1.92 µm) region. Normally, a gold-coated surface shows an increasing reflectivity of 65%–90% between 500 and 1000 nm and more than 90% at longer IR wavelengths. **Figure 8b** illustrates the non-linear response of Raman line intensity of the substrate without R6G with the probe power, where the intense lines occur between ≈ 500–1500 cm^{-1}. All materials generate a Raman spectrum, except for pure metals, which are highly reflective because of the free electrons on their surface. If a crystal is centrosymmetric, IR bands will not show up in the Raman spectrum and vice versa. An essential condition to obtain Raman spectra of samples is a change in polarizability during molecular vibration, and the metals do not show the polarizability change. As a result, metallic elements with the face-centered cubic (fcc) structure, such as gold, have no Raman-active vibrations. Therefore, the peaks shown in **Figure 8b** are considered the background spectral profile partly because of the presence of some impurities in the substrate.

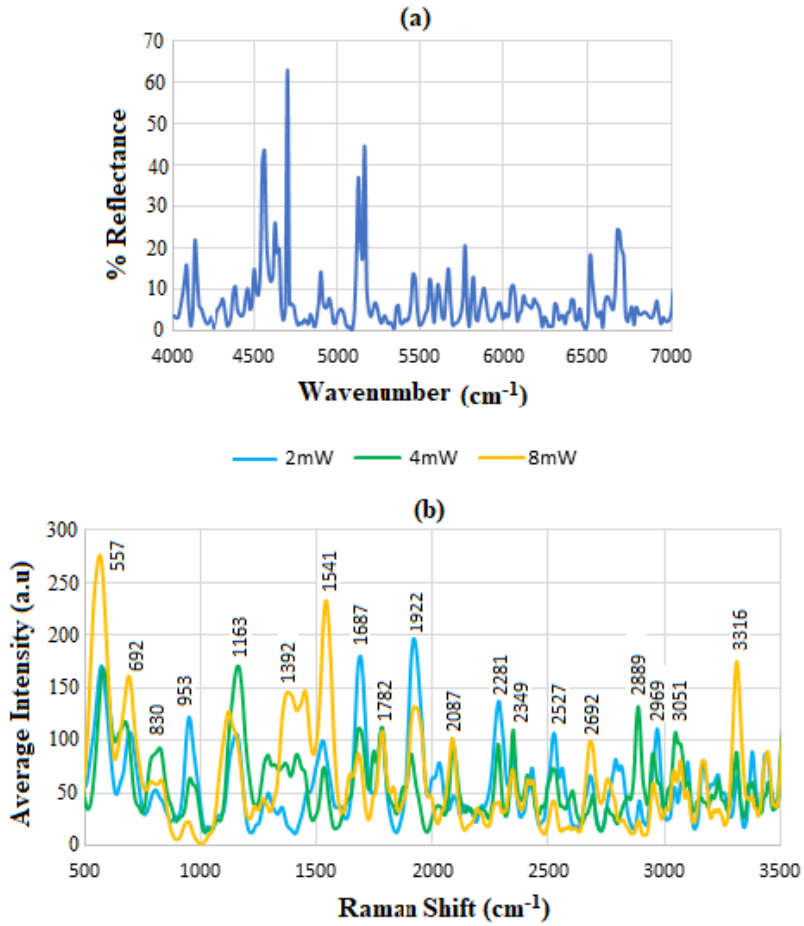

Figure 8. (a) FT-NIR reflectivity of the TGFS where most reflection occurs between 4000 and 5200 cm^{-1}, i.e., at shorter IR wavelengths, and **(b)** indicates the averaged Raman intensity at various laser powers.

Figure 9a shows the schematic representation of R6G dye added to the substrate, and **Figure 9b** illustrates the experimental setup where the beam travels through the sample droplet placed on the substrate. **Figure 9c** displays the SERS results of 10 mM R6G on TGFS at different power levels, showing significant fluctuations in the relative intensities of certain vibrational bands. It is noticed as expected that the intensity of the R6G Raman lines is enhanced compared to those in **Figure 6**. A common feature of molecular spectra is the variation of the temporal spectrum, which is mainly associated with a deviation from the ensemble average [53–55]. The fluctuation occurs due to varying charge transfer contributions caused by dynamic changes in the molecular environment, such as random movement of the molecule on the metallic surface during the adsorption [45].

The spectral fluctuations can be influenced by various physical and chemical properties of molecules and substrates, including diffusion, reorientation, adsorption, and desorption of the molecules. Indeed, it has been demonstrated that diffusive processes on the surface can cause molecules to experience continuously varying interaction forces that may result in the modulation of emission and control of the vibrational modes [56,57]. Additionally, environmental factors such as light and temperature, optical parameters like light intensity, and chemical factors including charge transfer have been shown to influence spectral fluctuations [58,59]. As shown

in **Figure 5**, the intensity of the scattered Raman lines, i.e., the population of vibrationally excited molecules, varies almost linearly with the laser power and is more intense at lower wavenumber, particularly between 500 and 1500 cm^{-1}, i.e., lower energy corresponding to aromatic modes of xanthene/phenyl rings, C-C rings [60], aromatic C-H bending, N-H in-plane modes, and C-C stretching modes [56,61]. The overall stochastic behavior of such spectral fluctuation has been observed previously [62,63], which is attributed to changes in the dynamic molecular environment or thermally activated diffusion of individual molecules [64]. The coupling between the vibrational modes and electronic states of R6G molecules and small changes in the position of adsorbed molecules on the TGFS and NPs can create a temporal modulation of these states, leading to the enhancement of the intensity of the analyte molecules. It has been suggested that in high-concentration analyte ensembles, these changes are normally masked by ensemble averages and therefore cannot be detected [55].

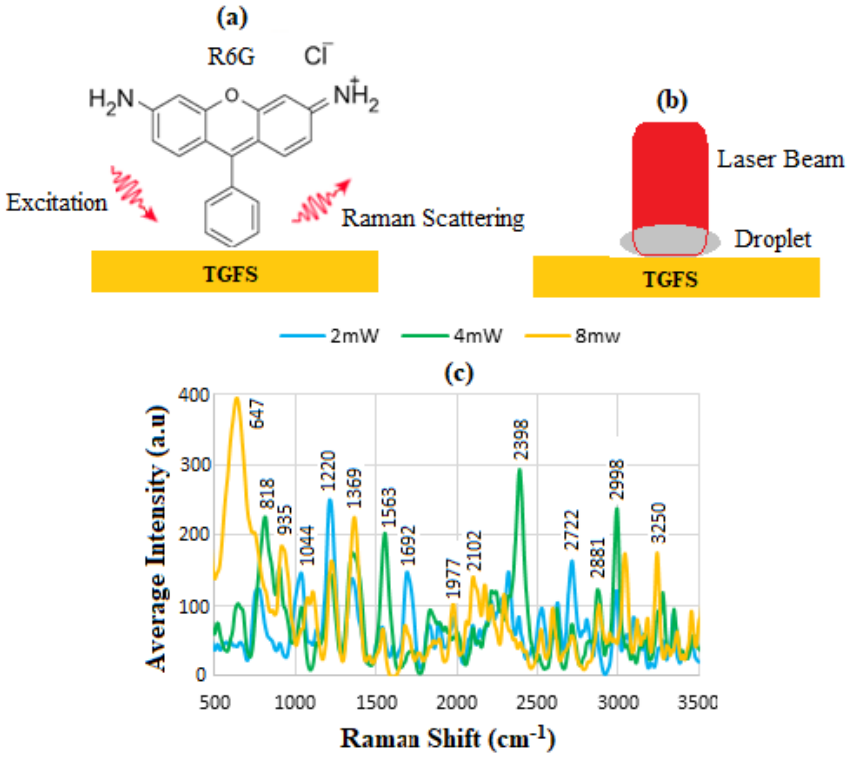

Figure 9. (a) Schematic representation of R6G dye SERS; **(b)** the experimental setup; **(c)** averaged SERS intensity of R6G at 10 mM.

The optical properties of gold thin films, along with the connection between the metallic thin films and the intrinsic characteristics of a plasmonic device, can be studied through the optical absorption of metal inter-band and intra-band electron transitions, as outlined by Drude's theory. For polycrystalline metal films, the electron scattering at surfaces and grain boundaries plays a great role in losses [65] and affects the complex dielectric constant of the metallic materials ε_m [66].

$$\varepsilon_m = \varepsilon_r + j\varepsilon_i = \varepsilon_\infty - \frac{\omega_p^2}{\omega^2 - i\gamma\omega} \quad (1)$$

$$\varepsilon_m = \varepsilon_\infty - \frac{\omega_p^2}{\omega^2 + \gamma^2} + \frac{\gamma\omega_p^2}{\omega(\omega^2 + \gamma^2)} \quad (2)$$

where the real part $\varepsilon_r = (n_s^2 - k_e^2)$ indicates the polarization of the metal in response to an applied external electric field, the imaginary part $j\varepsilon_i = 2n_s k_e = \gamma\omega_p^2/\omega(\omega^2 + \gamma^2)$ represents the optical absorption in metal, quantifying the relative phase shift of the induced polarization with respect to the external field, which includes losses such as ohmic loss as heat, ε_∞ is the infinite-frequency dielectric constant (i.e., the net electric field inside the metal is zero), γ is the damping factor, n_s is the refractive index of metal, and ω_p is the plasmon frequency defined as:

$$\omega_p^2 = \frac{n_e e^2}{m_{eff}\varepsilon_0} \quad (3)$$

where n_e is the density of electrons, e is the electron charge, ε_0 is the vacuum dielectric constant permittivity, and m_{eff} is the electron effective mass, respectively. Since the total field at the metal surface is $E_T = E_0(\omega) + E_s(\omega)$ where $E_s(\omega)$ in the dipolar mode, is given by [67].

$$E_s = \frac{(1+K)\varepsilon_e}{(\varepsilon_m + K\varepsilon_e)} E_0(\omega) \quad (4)$$

where K is the shape factor and ε_e is the dielectric constant of the surrounding environment. When a molecule is placed close to a surface, its scattering cross-section is significantly enhanced. A key aspect related to the origin of SERS is that the oscillating dipole moment μ_d of a plasmonic molecule re-radiates some of its energy at the same frequency as E_0.

After interacting with the laser, the molecule's associated field E_{μ_d} interacts with the incident light, causing it to scatter elastically.

This scattering produces an isotropic intensity distribution because the wavelets emitted by the oscillating charges are approximately in phase with one another [68].

$$\mu_d = 4\pi\varepsilon_m R_{mo}^3 \left(\frac{\varepsilon_{mo} - \varepsilon_{en}}{\varepsilon_{mo} + 2\varepsilon_{en}}\right) \bar{E}_0 e^{i\omega t} \quad (5)$$

where ε_{mo} and ε_{en} are the molecule and the medium dielectric constants, respectively, R_{mo} is the molecule radius, and ω is the field angular frequency. The intensity of the scattered light, I_s directly depends on the polarizability, α_p, which in turn depends on the molecular weight and on the particle size. Therefore, the higher a particle α_p, the greater will be the magnitude of induced μ_d and I_s. Since E_{μ_d} in the molecule is proportional to its volume V_{mo}, and I_s is proportional to V_{mo}^2, it follows that the intensity of reradiated light $I_r = \left|E_{\mu_d}\right|^2$ is proportional to V_{mo}^2 as well. Therefore, the scattered intensity will be stronger than at lower molecular weight or volume. Therefore, when a Raman scattering molecule is subject to an intense electric field generated near metal surfaces, the strong electric field intensity enhances the polarization on the molecule, leading to a higher induced μ_d [69,70]. **Figure 10a** is a schematic representation of hexane-functionalized TGFS immobilized by GNU via a simple covalent thiol bond, i.e., the PANTF structure. **Figure 10b** compares the

reflectivity of TGFS before and after GNU immobilization; the reflectivity significantly increases when GNU is added with the dominant lines of 1443, 1511, 1685, 1702, 2044, 2125, 2200, and 2397 nm (i.e., ≈ 4172–6930 cm^{-1}).

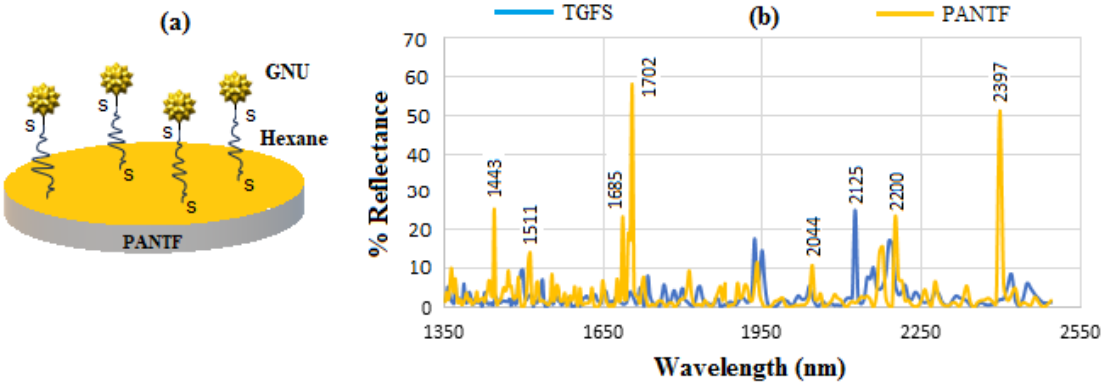

Figure 10. (a) Schematic of GNU immobilized on the hexane functionalized TGFS (i.e., PANTF) and **(b)** FT-NIR of PANTF.

Figure 11a shows the SERS of the TGFS due to its plasmonic properties, with the dominant Raman scattering observed at 2333 cm^{-1} corresponding to approximately ≈ 4.2 μm. It is known that metals do not produce strong Raman signals due to a lack of vibrational modes that can be excited by incident light. What is observed in **Figure 11a** is not the Raman signal but the enhancement of signals from molecules in close proximity. Homonuclear diatomic molecules are Raman active because the stretching and contraction of the bonds alter the interactions between the nuclei and electrons, causing a change in the molecule's polarizability. Thus, it is expected that Au(I), i.e., aurous ion, which is the most common oxidation state with soft ligands such as thioethers, thiolates, and organophosphines, may produce the above result. **Figure 11b** presents the SERS spectrum of GNU colloids, highlighting prominent peaks at 1475, 2314, 2590, 2696, and 2981 cm^{-1}, which are associated with citrate. Citrate acts as an intermediate in the citric acid cycle and plays a role in reducing gold ions into atoms, which helps stabilize the colloidal AuNPs formed from these aggregated atoms.

Generally, AuNPs are plasmonically active in the NIR region, making them suitable for biomedical applications because they exhibit minimal autofluorescence from biological samples. The primary factor contributing to the SERS enhancement is the increased intensity of inelastically scattered Raman signal due to the presence of nanostructured metal systems in the sample. Moreover, these particles enhance the morphological interaction with the incident laser, leading to more intense spectroscopic signals. The effect of probe power on the SERS lines of the PANTF is shown in **Figure 11c**, where the intensity is relatively enhanced due to the immobilization of GNU compared to those in **Figure 8b** of TGFS as background. The increase in the size of the GNU is attributed to conjugation via thiol bonds, which results in Raman vibrational scattering at higher frequencies. The SERS bands of hexane thiol are at 780 cm^{-1}, which is associated with CH_2 vibration; 935 cm^{-1} corresponds to the CH_3 rocking vibration, 1032 cm^{-1} and 1209 cm^{-1} indicate C-C cm^{-1} stretching vibration, while the bands at 1301 cm^{-1} and 1448 cm^{-1} are likely due to the CH_2 wagging vibration [71].

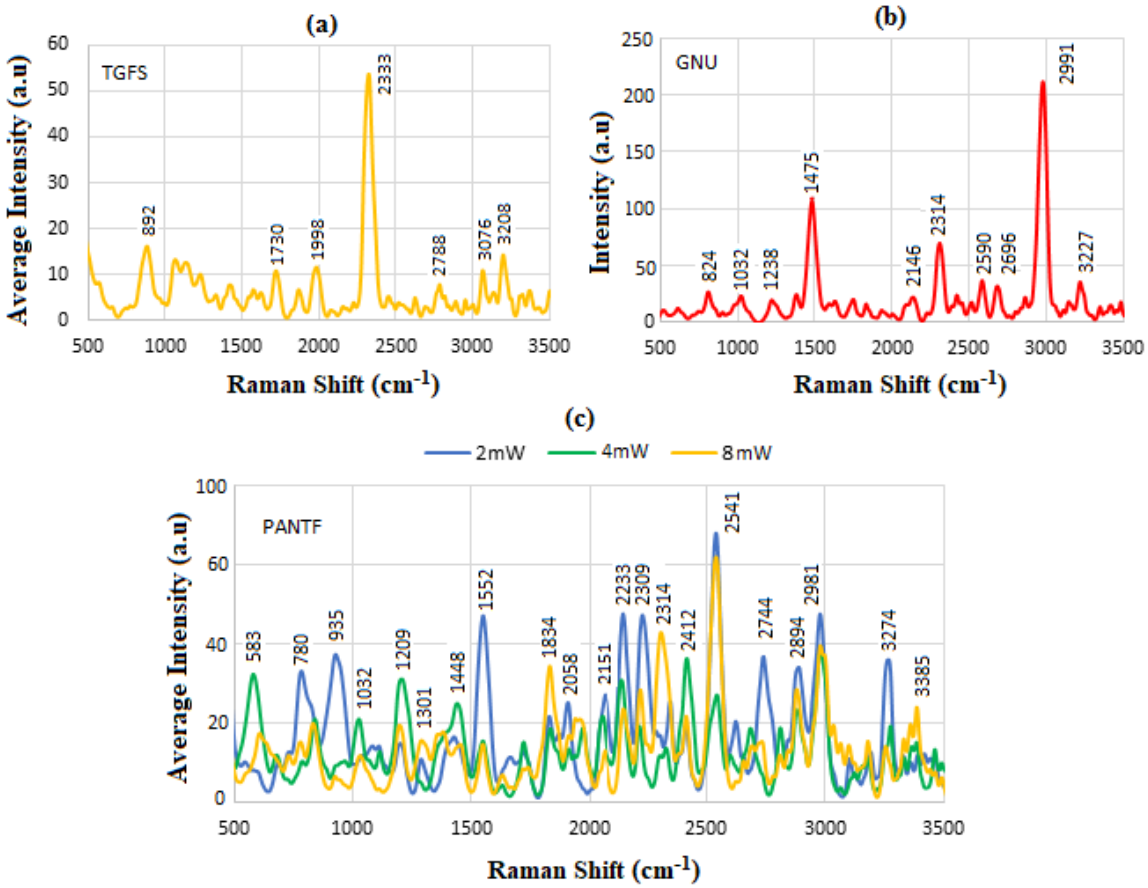

Figure 11. SERS of **(a)** TGFS, **(b)** GNU solution, and **(c)** PANTF at various probe power.

The GNU layer serves as hotspots within the adjacent irregular morphology of TGFS, enhancing the plasmon resonance effect for the detection of R6G through the LSPR mechanism. When the size of the NPs is much smaller than the incident wavelengths, the elastic scattering cross-section of the NP increases significantly, which leads to a strong enhancement of the local electromagnetic fields. Theoretical studies [56] have demonstrated that in a single NP-film system, the wavelength of surface plasmon polariton (SPP) remains unchanged. This is because the perturbation of the delocalized SPPs supported by an infinitely thin film is negligible, unlike in systems with a larger number of nanoparticles. In our SERS experiment, it is assumed that the laser directly excites the LSPR of GNUs but does not directly couple to the SPP of TGFS. This is due to a mismatch between the in-plane wavevectors of these mods and those of the incident photons that propagate through the air gap between the probe and the TGFS [72,73]. The GNU provides an indirect way to excite the SPPs of the TGFS across all wavelengths. This implies that GNU does not interact preferentially with any specific SPP; instead, it couples with the entire range of SPP modes. Therefore, the LSP scattering of GNUs transmits both into far-field, acting as a nano antenna, and into the non-resonant continuum of SPP modes within the TGFS, which further enhances the SERS signal and induces a polarization to the single nanoparticle light scattering [74].

Figure 12 illustrates SEM images of PANTF where the surface morphology exhibits a clustering feature, **Figure 12a**, where each cluster consists of a number of nanoparticles aggregated together. The clusters demonstrate various shapes and sizes,

which in turn will affect the SERS signal; some scratches and artifacts are also observed. At much higher magnification shown in **Figure 12b**, the clusters do not show the same smooth curve but instead an irregular and spiky shape similar to the geometrical shape of GNU is formed.

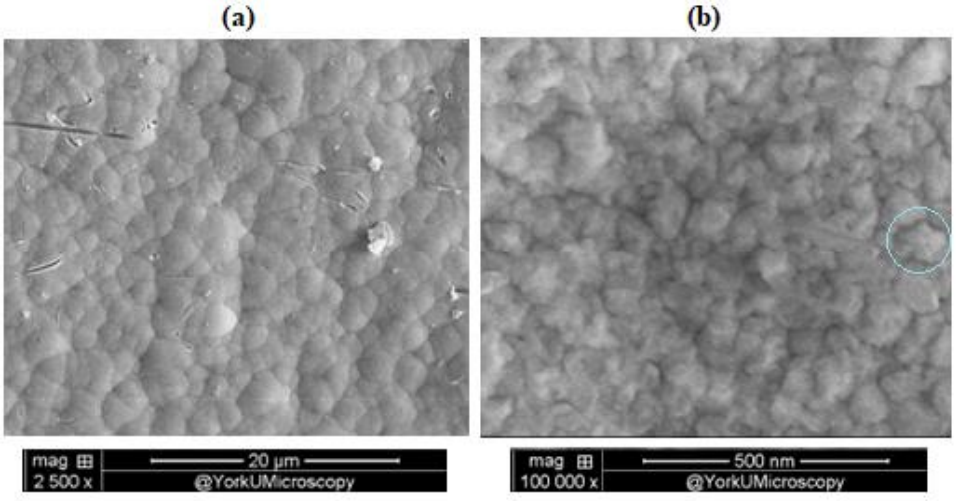

Figure 12. SEM images of PANTF at **(a)** low and **(b)** high magnification. The inset shows an example of a GNU particle that could not be seen in **(a)**.

The surface topography and roughness of PANTF were also investigated by AFM in non-contact scanning mode for a number of scans. The images were taken from the center of the chip at a 10 × 10 μm resolution, and a 3-D profile is associated. **Figure 13a,b** illustrate the 2-D surface morphology of PANTF, where the GNUs are aggregated together due to surface-attractive interactions to generate a larger cluster and have created an irregular topological feature on the surface. This effectively affects the surface roughness, which in turn affects the SERS signal because of a change in the surface plasmon probing depth between the analyte molecule and the substrate base. The brighter regions in the image are caused by the laser beam used to detect deflections of the cantilever either towards or away from the surface. When an incident beam reflects off the flat top of the cantilever, any deflection will cause small changes in the direction of the reflected beam. When the incident beam reflects off the flat top of the cantilever, any deflection will cause small changes in the direction of the reflected beam. The corresponding 3-D images are illustrated in **Figure 13c,d**. In these images, the previous spikes have nearly vanished due to coverage by GNUs.

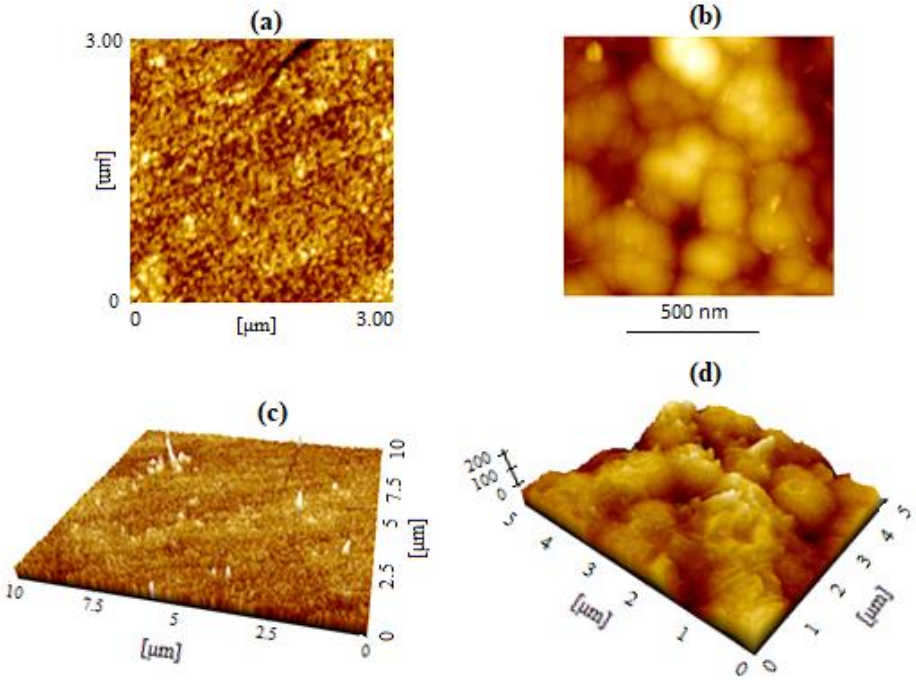

Figure 13. (a) and **(b)** 2D AFM images of PANTF where GNUs are partly aggregated and distributed on the surface; **(c)** and **(d)** are 3D images showing the irregular feature of the surface.

The final step was to study the SERS of R6G using PANTF as illustrated in **Figure 14a**, where the initial enhanced hexane Raman probe signal is coupled to that of the R6G to produce the final SERS signal. This is because GNU particles act as hotspots that amplify the plasmon resonance effect in R6G detection. This amplification is due to the increased light scattering cross-section when exposed to laser excitation [75]. The differential spectra indicate that R6G can be effectively used for SERS sensing. It is well known that SERS signals arise from a strong interaction between a molecule and its substrate. Furthermore, the spatial arrangement of these components significantly influences the electromagnetic and chemical enhancements observed in the Raman signal.

The variations in the recorded SERS signal are likely due to different charge transfer effects, which are probably caused by dynamic changes in the molecular environment. This includes the random movement of the molecule onto the metallic surface during the adsorption process [45]. Interactions of molecules and substrates, including adsorption, desorption, surface diffusion, and molecular reorientation, can influence fluctuations. Furthermore, the analyte molecules are likely located on the surface of the substrate rather than in between GNU hotspots. This placement impacts the reproducibility of SERS because the number of GNUs can vary from one position to another. As a result of this non-homogeneous distribution, signals are produced with varying intensities and levels of enhancement.

The variation of averaged SERS intensity (a total of three readings for each sample) of R6G using the 10 min incubated substrate with laser power is shown in **Figure 14b–d**, whereby increasing the power, the relative intensity increases, particularly at 8 mW. Certain lines, including 583, 641, 786, 799, 923 cm^{-1} in the low

wavenumbers range, as well as 2757, 2766, and 3254 cm^{-1} in the high wavenumbers range, are significantly enhanced by PANTF substrate.

In the range between 1500 and 2500 cm^{-1}, the intensity of both cases remains relatively low or unchanged, and a few lines, such as 1220, 1363, 1698, 2398, and 2933 cm^{-1} mainly corresponding to secondary and NH_3^+ amines, remained higher in the case of TGFS. It was noted that the NH_3^+ amine peak showed an increase in intensity when GNU was present, compared to when it was absent. However, the other R6G peaks associated with the benzoic ester and secondary amine functional groups did not exhibit the same level of enhancement. It is proposed that the NH_3^+ functional group underwent a notable enhancement as a result of the electrostatic interaction between its positive charge and the naturally occurring negative charge on GNU. Since the enhancement in SERS enhancement is dependent on distance, NH_3^+ showed the strongest enhancement due to its direct interaction with GNU. It was also noted that higher laser power resulted in a stronger intensity of both Raman and SERS peaks. Some slight shifts in the Raman lines were noted, particularly those associated with aromatic C-C stretching. These shifts may result from interactions between the substrates and the probe molecules. The molecules of R6G contain conjugated aromatic rings, which predispose $\pi - \pi$ to stack with GNU [76,77].

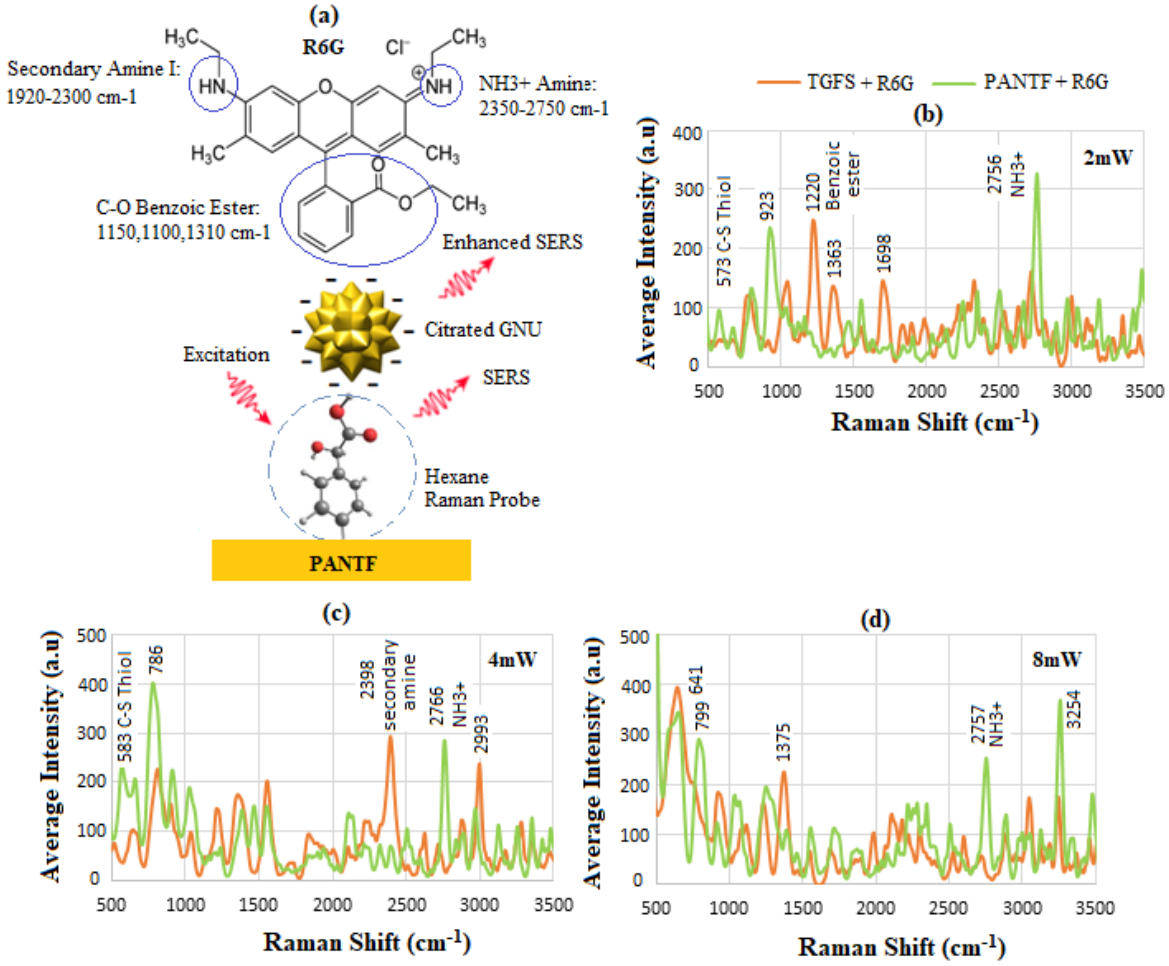

Figure 14. (a) Schematic diagram of enhanced SERS of R6G using PANTF after 10 min of incubation via thiol covalent bond, the corresponding Raman and SERS spectra of TGFS and PANTF are presented at **(b)** 2 mW, **(c)** 4 mW, and **(d)** 8 mW, respectively.

When using a 60 min PANTF, the results at 2 mW shown in **Figure 15a** are slightly worse compared to those in **Figure 14a**. In **Figure 14a**, the line intensity remains predominantly low across the spectrum except for two significant peaks at 2998 cm^{-1} and 3156 cm^{-1}. As the power increases, the Raman lines show a noticeable improvement across the spectrum, especially at 8 mW. One of the primary reasons for the varying profile patterns and reproducibility of SERS is a lack of surface stability in most enhancing material surfaces.

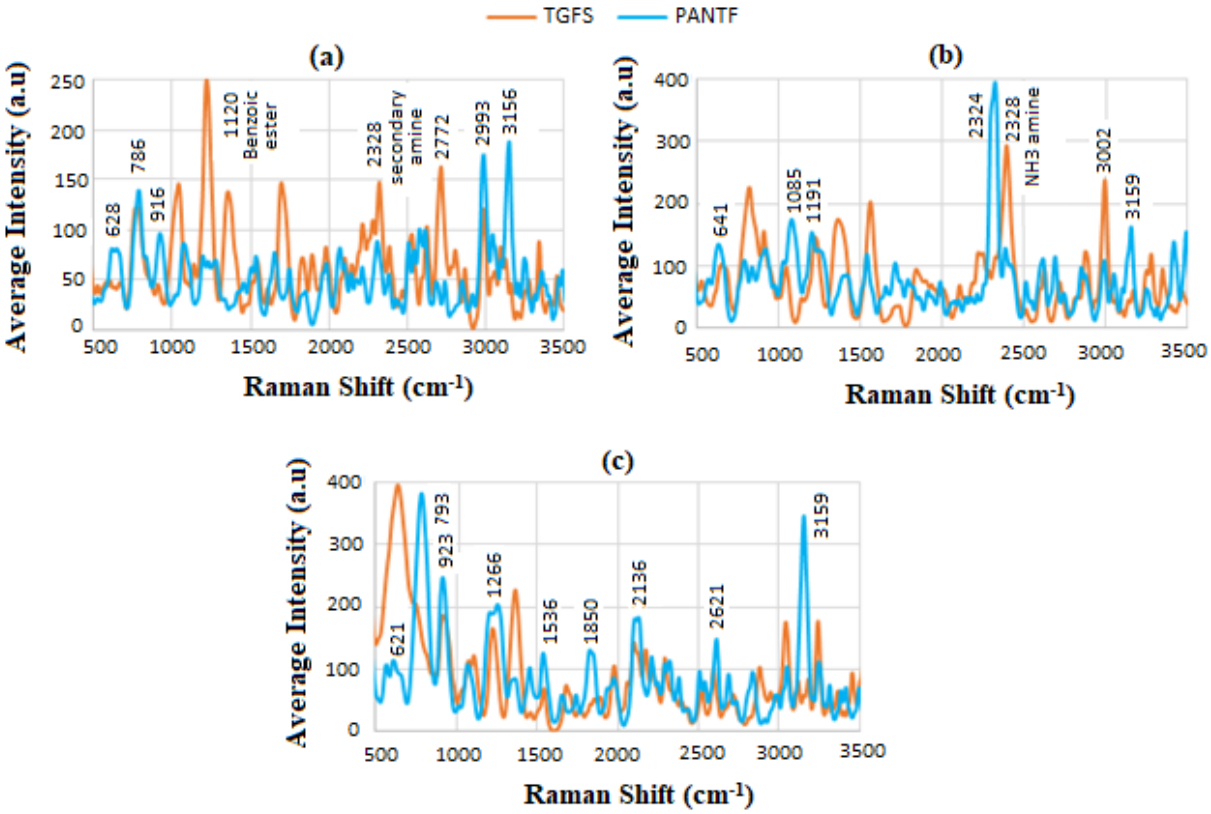

Figure 15. Schematic diagram of the enhanced SERS of R6G using PANTF after 60 min of GNU incubation through thiol covalent bond. The corresponding Raman and SERS spectra of TGFS and PANTF are presented at **(a)** 2 mW, **(b)** 4 mW, and **(c)** 8 mW, respectively.

Figure 16a shows the overlapped results related to the PANTF incubated for 10 min at various power levels, and similarly, the results for the 60 min incubation are shown in **Figure 16b**. It is noteworthy that as the power increases, the intensity behaves non-linearly at different spectral positions with increasing overall profiles. The positions at which the intensity of overlapped peaks increases linearly, such as 647 and 3258 cm^{-1} in **Figure 16a** and 923, 1232, and 3156 cm^{-1} in **Figure 16b**, the sensor can be utilized for monitoring the detection of analyte, in our case R6G.

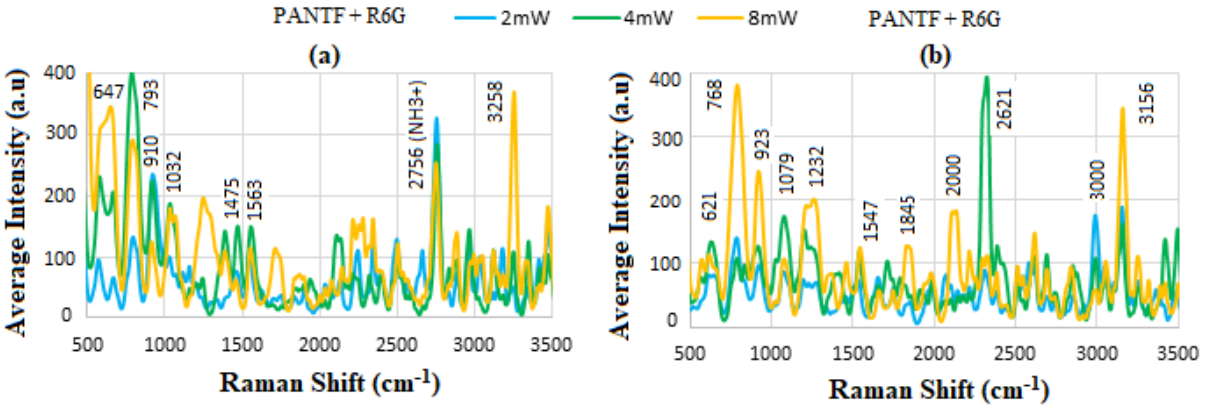

Figure 16. Comparison of overlapped peaks of PANTF for **(a)** 10 min and **(b)** 60 min incubation time.

Figure 9a illustrates the addition of 10 µL of a 10 mM solution of R6G, a Raman-active probe molecule, to the TFGS. The calculation is performed using $N = nN_A$ where $n = CV$ is the number of moles, C is the concentration, and V is the volume of the solution; N is the number of molecules, and N_A = 6.0224 × 10^{23} mol^{-1} is Avogadro's number. The corresponding values are n = 100 × 10^{-9} mol and N = 600 × 10^{14} R6G molecules, respectively. For PANTF, 10 µL of a 1 µM R6G solution was applied to the surface to accommodate the larger surface area of the GNU during the SERS measurements [35]. Similarly, we found corresponding values of n = 10 × 10^{-12} mol and N = 6 × 10^{12} molecules for SERS. The enhancement of line intensity due to LSPR is utilized to determine the EF at a specific power, as illustrated in **Figures 13** and **14** and calculated using Equation (6), which is summarized in **Tables 2** and **3**.

$$EF = \frac{I_{SERS}}{I_{Raman}} \times \frac{C_{Raman}}{C_{SERS}} \quad (6)$$

where I_{Raman} is the intensity of the bare substrate with R6G at concentration C_{Raman} = 10 mM, I_{SERS} is the intensity of the GNU-immobilized substrate with R6G at concentration C_{SERS} = 1 µM, so $\frac{C_{Raman}}{C_{SERS}}$ = 10^4. Substituting the above values given in **Table 2** in Equation (6), we obtain EF = 3 × 10^4 for all three 10 min incubation PANTF substrates at various powers, and similarly, using the corresponding values of intensity for RS and SERS in **Table 3**, it yields corresponding average values of 0.9 × 10^4, 2.1 × 10^4, and 1.1 × 10^4 for 60 min PANTF substrates, respectively.

Table 2. Peaks used to determine the average value of EF for 10 min incubation PANTAF at the various power levels based on **Figure 13**.

Common Peaks (cm^{-1})	RS Intensity	SERS Intensity	*EF* Value
573	40.69	80.73	1 × 10^4
923	30.41	230.32	6 × 10^4
1220	240.82	30.51	1 × 10^3
2757	60.68	320.62	4 × 10^4
Average *EF*, **Figure 13a**			3 × 10^4

Table 2. (*Continued*).

Common Peaks (cm^{-1})	RS Intensity	SERS Intensity	*EF* Value
583	30.63	220.14	6×10^4
786	170.62	400.07	2×10^4
2398	280.84	40.55	1×10^3
2766	30.21	270.28	8×10^4
2993	230.40	60.68	2×10^3
Average *EF*, **Figure 13b**			3×10^4
641	390.51	340.44	8×10^3
799	130.54	280.14	2×10^4
1375	210.96	90.71	4×10^3
2757	20.14	240.81	1×10^5
3254	120.47	350.62	2×10^4
Average *EF*, **Figure 13c**			3×10^4

Table 3. Peaks used to determine the average value of EF for 60 min incubation PANTF at the various power levels based on **Figure 14**.

Common Peaks (cm^{-1})	RS Intensity	SERS Intensity	*EF* Value
628	40.32	7046	2×10^4
1220	240.82	60.11	2×10^4
2328	140.26	80.17	6×10^4
2722	150.96	200.10	1×10^4
2998	100.92	160.46	2×10^4
Average *EF*, **Figure 14a**			0.9×10^4
641	90.70	120.63	1.3×10^4
2328	90.06	390.52	4.4×10^4
3003	220.72	100.49	0.5×10^4
Average *EF*, **Figure 14b**			2.1×10^4
653	380.07	100.89	3×10^4
1238	160.47	180.98	1.1×10^4
2621	70.65	140.10	2×10^4
Average *EF*, **Figure 14c**			1.1×10^4

A single nanoparticle (NP) typically does not provide sufficient EF for SM-SERS, and only the gaps between nanoparticles are active. It has been demonstrated that only the aggregation of multiple nanoparticles can provide enough EF for SM-SERS [78–80]. Each nanostructured TGFS has a different morphology with a certain number of NPs of various sizes acting as dipoles and multipoles under an applied field, and shapes, both of which depend on the thickness of the thin films [81]. In the case of the thinner film, there is more unoccupied space by NPs with no or very little scattering, and as the film thickness increases, the empty space becomes more occupied by NPs. This in turn increases the NP-NP interaction in the films due to a decrease in the inter-particle separation, thus causing the higher scattering, i.e., increased intensity of SERS, thus EF. The inter-particle distance, i.e., hot spots, can

vary either due to an increase in number density or an increase in the size of AuNPs, which contributes to the variation of SERS intensity [73]. When the analyte molecule is positioned in the gap between the NPs, the Raman scattering is significantly enhanced. Research has demonstrated that the enhancement is most significant when the interparticle gap is less than 15 nm [82]. The relatively low EF may be attributed to several reasons, including variation in the spatial distribution of enhancements at hot spots and issues related to photobleaching. This is a photophysical phenomenon wherein a dye or a fluorophore molecule undergoes permanent chemical damage caused by prolonged laser (or non-laser) excitation, hence cleaving covalent bonds or non-specific reactions between the fluorophore and surrounding molecules. As a result, the dye loses its functionality.

It is well-established that as temperature rises, the diffusion and randomness of molecules also increase. The solution to the 1-D random walk is expressed as the average of the square of the displacement $\overline{x^2} = 2Dt$, where D represents the Fick's diffusion coefficient (m^2/s). This coefficient is defined by the Stokes-Einstein equation, which indicates that a larger $\overline{x^2}$ corresponds to greater diffusion. As a result, raising the temperature due to the increase in power increases the molecular fluctuations within the medium. As a result, the temperature gradient can drive the analyte molecules out of confined spaces, leading to microscale movement driven by thermal diffusion and convection. The overall effect impacts the molecular distribution, resulting in varying concentrations at different positions, which in turn generates the corresponding SERS signal. The signal is stronger when the combined forces are balanced, causing the laser to irradiate areas with higher particle concentration. It weakens when the particles are dispersed or depleted from the hotspot, where the localized coupled plasmon resonance occurs between two or more PNP [83,84].

Some molecules on the substrate are also susceptible to photodecomposition at high laser power, creating so-called dynamic species change over time [14]. The microscopic temperature gradient and radiation pressure can propel the analyte molecules and the NPs out of the confined regions, resulting in microscale movement driven by the photo-thermophoresis force. This movement can redistribute their concentrations on the surface, ultimately influencing the final SERS results [85–87].

The heating effect can cause the degradation of the hot spot, trigger molecular desorption, or initiate pyrolysis. These outcomes may lead to a reduction in the SERS signal and its instability. The difference in the SERS spectra could be attributed to variations in scattered light at different power levels, affecting the intensity, $I = |\bar{E}|^2$. Additionally, the heating effect on the molecules at the microscale, such as thermally induced fluctuation or diffusion of dynamical changes in the microenvironment, may play a role. According to quasi-classical thermodynamics, these effects could be stochastic in nature. Another interesting reason is related to the NP-Film distance, where the spectral response interplay between LSP and SPP, for short separations (0–50 nm), the coupling between them can create significant enhancement, and at larger distances, LSP and SPP resonances overlap [72].

The concentrated Raman signal stems from the tips or junctions of GNU, where field enhancement is most significant, and possibly from the interstitial sites between

the core and tips of the GNU [88,89]. At certain binding sites, a red shift may occur due to the increasing size of the nanocomplex. This leads to greater retardation of multi-scattering and dispersion, which are influenced by the R6G molecular coating and the varying sizes of the GNU [90]. Therefore, the clustering of GNU leads to Mie scattering, causing the scattered light to shift to a longer wavelength and lower energy. Indeed, I_{SERS} depends on the number of molecules within the vicinity of 0.1–1 nm to metallic nanostructures in the position of the laser excitation spot. It has been suggested that one evidence for SM behavior is the spectral changes during the observation and that the photochemical and photobleaching is significantly decreased. This is due to the rapidly quenched excited electronic state by the metal surface, thus preventing excited state reactions. It was noticed during the experiment that some of the observed SERS signals vanished or changed after irradiation for a longer time. There are several factors that contribute to the varying intensities observed in SERS, one of which is the presence of hot spots, which occur at the junctions or close interactions between two or more NPs. Therefore, when GNUs are chemisorbed onto a substrate with a lower D/R_p ratio, they should display stronger resonance coupling. This is due to plasmonic interactions between NPs at high surface densities, which leads to the formation of more pronounced hot spots and, as a result, an enhancement of SERS signals [46,91,92]. Agglomerates can have hot spots, with characteristics depending on the shape and size of the built unit. Increasing the separation between the GNU cores decouples the corresponding SPR, thereby decreasing the EF. The overall SERS intensity $I(\omega_R)$ can be expressed as [3].

$$I(\omega_R) = \eta E_{ind} |\alpha_R(\omega_R, \omega_0)|^2 I_0(r, \omega_0) \tag{7}$$

where the collection efficiency of the device is

$$\eta = \left[\frac{E_l(r, \omega_0)}{E_0(r, \omega_0)}\right]^2 \left[\frac{E_l(r, \omega_R)}{E_0(r, \omega_R)}\right]^2 \tag{8}$$

E_{ind} is the electromagnetic-induced enhancement, ω_0 is the frequency of excitation photons, ω_R is the frequency of Raman photons, $\alpha_R(\omega_R, \omega_0)$ is the Raman polarizability of the molecule, and $I_0(r, \omega_0)$ is the intensity of the excitation light. Polarizability can impact dispersion forces, the weakest type of intermolecular force, in several ways, including enhancing the polarizability and being influenced by the shape of the molecule. Elongated molecules have electrons that move easily, which increases their polarizability and strengthens the dispersion forces. Additionally, GNU is sensitive to polarization because its branches create different dipole moments. The spatial charge distribution in each branch can produce individual dipoles pointing in various directions on the GNU [93,94], and alter could change the spatial thermal distribution when heated [14]. The scattering response of a single GNU is strongly polarized when excited at SPR wavelength. The polarization dependence of the scattering intensity, which suggests that surface plasmon resonance behaves like a single dipole scatterer, can have a significant impact on the results of SERS [95]. Thus, the SERS signals from different substrates differ with wavenumber, which corresponds to the wavelength of the emitted radiation. This variation represents the molecular rotational and vibrational energy of specific chemical bonds, as well as the overall chemical composition.

6. Conclusions

The preliminary study demonstrated a higher intensity of R6G Raman lines for TGFS compared to the R6G solution alone. The surface morphology of the GNU-immobilized TGFS was analyzed using SEM and AFM. It was shown that PANTF can relatively improve the SERS results compared to TGFS due to LSPR contribution. The results showed a stronger Raman response for R6G at higher concentrations, and TGFS and PANTF indicated an enhanced signal compared to R6G alone. The PANTF incubated with GNU at 10 min exhibited moderately better SERS results than TGFS, particularly at low wavenumbers such as the overlapped single peak at 647 cm^{-1} corresponding to C-C-C ring in-plane bending in Xanthene/phenyl. However, the results deteriorated when incubated for a longer time (60 min) and became comparable to TGFS results. The EF for 10 min was higher than 60 min incubation. Two key features were consistently observed throughout the experiments. First, there was a variation in the Raman shift signal, which indicated changes in molecular vibrations. Secondly, the signal exhibited a non-linear response to the probe power. Lastly, the sensitivity of the PANTF sensor can be enhanced by further optimizing the film thickness, GNU size, concentration, and incubation time.

Author contributions: Supervision, MEK; conceptualization, MEK; investigation, MEK; data curation, MEK, YP and CG; formal analysis, MEK; methodology, MEK, YP and CG; writing—original draft, MEK; validation, YP, CG and VU; review and editing, CG; signal processing, VU. All authors have read and agreed to the published version of the manuscript.

Acknowledgments: The authors would like to thank the MIS Electronics Inc. for supporting and funding the research for Nanobiophotonic and Biomedical Research Lab.

Institutional review board statement: Not applicable.

Informed consent statement: Not applicable

Data availability: The data that support the findings of this study are available within the manuscript.

Conflict of interest: The authors declare no conflict of interest.

References

1. Betzig E, Chichester RJ. Single Molecules Observed by Near-Field Scanning Optical Microscopy. Science. 1993; 262(5138): 1422-1425. doi: 10.1126/science.262.5138.1422
2. Macklin JJ, Trautman JK, Harris TD, et al. Imaging and Time-Resolved Spectroscopy of Single Molecules at an Interface. Science. 1996; 272(5259): 255-258. doi: 10.1126/science.272.5259.255
3. Qiu Y, Kuang C, Liu X, et al. Single-Molecule Surface-Enhanced Raman Spectroscopy. Sensors. 2022; 22(13): 4889. doi: 10.3390/s22134889
4. He S, Chua J, Tan EKM, et al. Optimizing the SERS enhancement of a facile gold nanostar immobilized paper-based SERS substrate. RSC Advances. 2017; 7(27): 16264-16272. doi: 10.1039/c6ra28450g
5. Szekeres GP, Kneipp J. SERS Probing of Proteins in Gold Nanoparticle Agglomerates. Frontiers in Chemistry. 2019; 7. doi: 10.3389/fchem.2019.00030

6. Hanna K, Krzoska E, Shaaban A, et al. Raman spectroscopy: Current applications in breast cancer diagnosis, challenges and future prospects. British Journal of Cancer. 2022; 126: 1125-1139. doi: 10.1038/s41416-021-01659-5
7. Khosroshahi ME, Chabok R, Chung N, et al. Optimization of immersion direction and time of covalently self-assembled monolayer gold nanourchins on glass as SERS substrate. Journal of Nanoparticle Research. 2023; 25(5). doi: 10.1007/s11051-023-05741-2
8. Shera EB, Seitzinger NK, Davis LM, et al. Detection of single fluorescent Molecules. Chemistry Physics Letter. 1990; 174(6): 553-557. doi: 10.1016/0009-2614(90)85485-U
9. Eigen M, Rigler R. Sorting single molecules: application to diagnostics and evolutionary biotechnology. Proceedings of the National Academy of Sciences. 1994; 91(13): 5740-5747. doi: 10.1073/pnas.91.13.5740
10. Krug JT, Wang GD, Emory SR, et al. Efficient Raman Enhancement and Intermittent Light Emission Observed in Single Gold Nanocrystals. Journal of the American Chemical Society. 1999; 121(39): 9208-9214. doi: 10.1021/ja992058n
11. Kneipp K, Kneipp H, Manoharan R, et al. Extremely Large Enhancement Factors in Surface-Enhanced Raman Scattering for Molecules on Colloidal Gold Clusters. Applied Spectroscopy. 1998; 52(12): 1493-1497. doi: 10.1366/0003702981943059
12. Ambrose WP, Goodwin PM, Martin JC, et al. Alterations of single molecule fluorescence lifetimes in near-field optical microscopy. Science. 1994; 265(5170): 364-367. doi: 10.1126/science.265.5170.364
13. Ha T, Enderle T, Ogletree DF, et al. Probing the interaction between two single molecules: fluorescence resonance energy transfer between a single donor and a single acceptor. Proceedings of the National Academy of Sciences. 1996; 93(13): 6264-6268. doi: 10.1073/pnas.93.13.6264
14. Blackie EJ, Le Ru EC, Etchegoin PG. Single-Molecule Surface-Enhanced Raman Spectroscopy of Nonresonant Molecules. Journal of the American Chemical Society. 2009; 131(40): 14466-14472. doi: 10.1021/ja905319w
15. Lin J, Huang Z, Lin X, et al. Rapid and label-free urine test based on surface-enhanced Raman spectroscopy for the non-invasive detection of colorectal cancer at different stages. Biomedical Optics Express. 2020; 11(12): 7109. doi: 10.1364/boe.406097
16. Khosroshahi ME, Patel Y, Umashanker V, et al. Fabrication of and characterization of directional antibody-conjugated gold nanourchin colloid and effect of laser polarization on SERS detection of breast cancer biomarker in serum. Colloids and Surfaces A: Physicochemical and Engineering Aspects. 2024; 694: 134035. doi: 10.1016/j.colsurfa.2024.134035
17. Willets KA, Van Duyne RP. Localized Surface Plasmon Resonance Spectroscopy and Sensing. Annual Review of Physical Chemistry. 2007; 58(1): 267-297. doi: 10.1146/annurev.physchem.58.032806.104607
18. Petryayeva E, Krull UJ. Localized surface plasmon resonance: Nanostructures, bioassays and biosensing—A review. Analytica Chimica Acta. 2011; 706(1): 8-24. doi: 10.1016/j.aca.2011.08.020
19. Jain PK, Lee KS, El-Sayed IH, et al. Calculated Absorption and Scattering Properties of Gold Nanoparticles of Different Size, Shape, and Composition: Applications in Biological Imaging and Biomedicine. The Journal of Physical Chemistry B. 2006; 110(14): 7238-7248. doi: 10.1021/jp057170o
20. Noguez C. Surface Plasmons on Metal Nanoparticles: The Influence of Shape and Physical Environment. The Journal of Physical Chemistry C. 2007; 111(10): 3806-3819. doi: 10.1021/jp066539m
21. Hassannejad Z, Khosroshahi ME. Synthesis and evaluation of time dependent optical properties of plasmonic–magnetic nanoparticles. Optical Materials. 2013; 35(3): 644-651. doi: 10.1016/j.optmat.2012.10.019
22. Khlebtsov B, Zharov V, Melnikov A, et al. Optical amplification of photothermal therapy with gold nanoparticles and nanoclusters. Nanotechnology. 2006; 17(20): 5167-5179. doi: 10.1088/0957-4484/17/20/022
23. Huang X, Jain PK, El-Sayed IH, et al. Gold Nanoparticles: Interesting Optical Properties and Recent Applications in Cancer Diagnostics and Therapy. Nanomedicine. 2007; 2(5): 681-693. doi: 10.2217/17435889.2.5.681
24. Otto A, Mrozek I, Grabhorn H, et al. Surface-enhanced Raman scattering. Journal of Physics: Condensed Matter. 1992; 4(5): 1143-1152. doi: 10.1088/0953-8984/4/5/001
25. Rodríguez-Oliveros R, Sánchez-Gil JA. Gold nanostars as thermoplasmonic nanoparticles for optical heating. Optics Express. 2011; 20(1): 621. doi: 10.1364/oe.20.000621
26. Hao F, Nehl CL, Hafner JH, et al. Plasmon Resonances of a Gold Nanostar. Nano Letters. 2007; 7(3): 729-732. doi: 10.1021/nl062969c
27. Pallavicini P, Donà A, Casu A, et al. Triton X-100 for three-plasmon gold nanostars with two photothermally active NIR (near IR) and SWIR (short-wavelength IR) channels. Chemical Communications. 2013; 49(56): 6265. doi: 10.1039/c3cc42999g

28. Khosroshahi ME, Patel Y. Reflective FT-NIR and SERS studies of HER-II breast cancer biomarker using plasmonic-active nanostructured thin film immobilized oriented antibody. Journal of Biophotonics. 2022; 16(3). doi: 10.1002/jbio.202200252
29. Taylor AD, Lu C, Geyer S, et al. Thin film based plasmon nanorulers. Applied Physics Letters. 2016; 109(1). doi: 10.1063/1.4955036
30. Hutter T, Huang FM, Elliott SR, et al. Near-Field Plasmonics of an Individual Dielectric Nanoparticle above a Metallic Substrate. The Journal of Physical Chemistry C. 2013; 117(15): 7784-7790. doi: 10.1021/jp400963f
31. Baumberg JJ, Aizpurua J, Mikkelsen MH, et al. Extreme nanophotonics from ultrathin metallic gaps. Nature Materials. 2019; 18: 668-678. doi: 10.1038/s41563-019-0290-y
32. de Barros A, Shimizu FM, de Oliveira CS, et al. Dynamic Behavior of Surface-Enhanced Raman Spectra for Rhodamine 6G Interacting with Gold Nanorods: Implication for Analyses under Wet versus Dry Conditions. ACS Applied Nano Materials. 2020; 3(8): 8138-8147. doi: 10.1021/acsanm.0c01530
33. Burtsev V, Miliutina E, Ulbrich P, et al. Immobilization of Gold Nanoparticles in Localized Surface Plasmon Polariton-Coupled Hot Spots via Photolytic Dimerization of Aromatic Amine Groups for SERS Detection in a Microfluidic Regime. ACS Applied Nano Materials. 2022; 5(2): 1836-1844. doi: 10.1021/acsanm.1c03413
34. Ma H, Zhang S, Yuan G, et al. Surface-enhanced Raman spectroscopy (SERS) activity of gold nanoparticles Prepared using an automated loop flow reactor. Applied Spectroscopy. 2023; 77(10): 1163-1172. doi: 10.1177/00037028231196907
35. Kau J, Chen X, Chin C, et al. Silver Nanocube-Decorated PVDF Membranes for SERS Substrates. ACS Applied Nano Materials. 2023; 6(11): 9148-9158. doi: 10.1021/acsanm.3c00202
36. Fu J, Zhang H, Xiang Z, et al. Biologically Inspired Superwetting Surface Enhanced Raman Scattering (SERS) Substrates. ACS Applied Nano Materials. 2024; 7(20): 23337-23367. doi: 10.1021/acsanm.4c04342
37. Tang J, Hao J, Li Z, et al. Towards understanding hybrid influencing mechanisms of substrate microstructure on SERS effect. Applied Surface Science. 2024; 660: 159974. doi: 10.1016/j.apsusc.2024.159974
38. Suzuki M, Niidome Y, Kuwahara Y, et al. Surface-Enhanced Nonresonance Raman Scattering from Size- and Morphology-Controlled Gold Nanoparticle Films. The Journal of Physical Chemistry B. 2004; 108(31): 11660-11665. doi: 10.1021/jp0490150
39. Atta S, Canning AJ, Vo-Dinh T. A simple low-cost flexible plasmonic patch based on spiky gold nanostars for ultra-sensitive SERS sensing. The Analyst. 2024; 149(7): 2084-2096. doi: 10.1039/d3an02246c
40. Pal A, Varma MM. Study of Surface-enhanced Raman scattering of Rhodamine 6G from repeated dewetted gold thin film. In: Proceedings of 2024 IEEE Applied Sensing Conference (APSCON); 22–24 January 2024; Goa, India.
41. Ujihara M, Dang N, Imae T. Surface-Enhanced Resonance Raman Scattering of Rhodamine 6G in Dispersions and on Films of Confeito-Like Au Nanoparticles. Sensors. 2017; 17(11): 2563. doi: 10.3390/s17112563
42. Cheong Y, Kim YJ, Kang H, et al. Rapid label-free identification of Klebsiella pneumoniae antibiotic resistant strains by the drop-coating deposition surface-enhanced Raman scattering method. Spectrochimica Acta Part A: Molecular and Biomolecular Spectroscopy. 2017; 183: 53-59. doi: 10.1016/j.saa.2017.04.044
43. Payne EK, Rosi NL, Xue C, et al. Sacrificial Biological Templates for the Formation of Nanostructured Metallic Microshells. Angewandte Chemie International Edition. 2005; 44(32): 5064-5067. doi: 10.1002/anie.200500988
44. Hrelescu C, Sau TK, Rogach AL, et al. Selective Excitation of Individual Plasmonic Hotspots at the Tips of Single Gold Nanostars. Nano Letters. 2011; 11(2): 402-407. doi: 10.1021/nl103007m
45. Indrasekara ASDS, Meyers S, Shubeita S, et al. Gold nanostar substrates for SERS-based chemical sensing in the femtomolar regime. Nanoscale. 2014; 6(15): 8891-8899. doi: 10.1039/c4nr02513j
46. Su KH, Wei QH, Zhang X, et al. Interparticle Coupling Effects on Plasmon Resonances of Nanogold Particles. Nano Letters. 2003; 3(8): 1087-1090. doi: 10.1021/nl034197f
47. Li R, Li H, Pan S, et al. Surface-enhanced Raman scattering from rhodamine 6G on gold-coated self-organized silicon nanopyramidal array. Journal of Materials Research. 2013; 28(24): 3401-3407. doi: 10.1557/jmr.2013.352
48. Sil S, Kuhar N, Acharya S, et al. Is Chemically Synthesized Graphene 'Really' a Unique Substrate for SERS and Fluorescence Quenching? Scientific Reports. 2013; 3(1). doi: 10.1038/srep03336
49. Wahadoszamen Md, Rahaman A, Hoque NMdR, et al. Laser Raman Spectroscopy with Different Excitation Sources and Extension to Surface Enhanced Raman Spectroscopy. Journal of Spectroscopy. 2015; 2015: 1-8. doi: 10.1155/2015/895317
50. Zhang Y, Zheng, guo, et al. Biosynthesis of gold nanoparticles using chloroplasts. International Journal of Nanomedicine. 2011: 2899. doi: 10.2147/ijn.s24785

51. Huang D, Cui J, Chen X. A morpholinium surfactant crystallization induced formation of Au nanoparticle sheet-like assemblies with uniform SERS activity. Colloids and Surfaces A: Physicochemical and Engineering Aspects. 2014; 456: 100-107. doi: 10.1016/j.colsurfa.2014.05.027
52. Zhong F, Wu Z, Guo J, et al. Porous Silicon Photonic Crystals Coated with Ag Nanoparticles as Efficient Substrates for Detecting Trace Explosives Using SERS. Nanomaterials. 2018; 8(11): 872. doi: 10.3390/nano8110872
53. Wu CY, Huang CC, Jhang JS, et al. Hybrid surface-enhanced Raman scattering substrate from gold nanoparticle and photonic crystal: Maneuverability and uniformity of Raman spectra. Optics Express. 2009; 17(24): 21522. doi: 10.1364/oe.17.021522
54. Basche T, Moerner WE, Orrite M, et al. Single-molecule optical detection, imaging and spectroscopy. Wiley-VCH; 1996.
55. Donhauser ZJ, Mantooth BA, Kelly KF, et al. Conductance Switching in Single Molecules Through Conformational Changes. Science. 2001; 292(5525): 2303-2307. doi: 10.1126/science.1060294
56. Xu H, Bjerneld EJ, Käll M, et al. Spectroscopy of Single Hemoglobin Molecules by Surface Enhanced Raman Scattering. Physical Review Letters. 1999; 83(21): 4357-4360. doi: 10.1103/physrevlett.83.4357
57. Weiss A, Haran G. Time-Dependent Single-Molecule Raman Scattering as a Probe of Surface Dynamics. The Journal of Physical Chemistry B. 2001; 105(49): 12348-12354. doi: 10.1021/jp0126863
58. Galloway CM, Le Ru EC, Etchegoin PG. Single-molecule vibrational pumping in SERS. Physical Chemistry Chemical Physics. 2009; 11(34): 7372. doi: 10.1039/b904638k
59. Emory SR, Jensen RA, Wenda T, et al. Re-examining the origins of spectral blinking in single-molecule and single-nanoparticleSERS. Faraday Discuss. 2006; 132: 249-259. doi: 10.1039/b509223j
60. Miranda AM, Castilho-Almeida EW, Martins Ferreira EH, et al. Line shape analysis of the Raman spectra from pure and mixed biofuels esters compounds. Fuel. 2014; 115: 118-125. doi: 10.1016/j.fuel.2013.06.038
61. He XN, Gao Y, Mahjouri-Samani M, et al. Surface-enhanced Raman spectroscopy using gold-coated horizontally aligned carbon nanotubes. Nanotechnology. 2012; 23(20): 205702. doi: 10.1088/0957-4484/23/20/205702
62. Jiang, Bosnick K, Maillard M, et al. Single Molecule Raman Spectroscopy at the Junctions of Large Ag Nanocrystals. The Journal of Physical Chemistry B. 2003; 107(37): 9964-9972. doi: 10.1021/jp034632u
63. Bizzarri AR, Cannistraro S. Lévy Statistics of Vibrational Mode Fluctuations of Single Molecules from Surface-Enhanced Raman Scattering. Physical Review Letters. 2005; 94(6). doi: 10.1103/physrevlett.94.068303
64. Ruan C, Wang W, Gu B. Single-molecule detection of thionine on aggregated gold nanoparticles by surface enhanced Raman scattering. Journal of Raman Spectroscopy. 2007; 38(5): 568-573. doi: 10.1002/jrs.1691
65. Sotelo J, Ederth J, Niklasson G. Optical properties of polycrystalline metallic films. Physical Review B. 2003; 67(19). doi: 10.1103/physrevb.67.195106
66. Qian H, Xiao Y, Lepage D, et al. Quantum Electrostatic Model for Optical Properties of Nanoscale Gold Films. Nanophotonics. 2015; 4(4): 413-418. doi: 10.1515/nanoph-2015-0022
67. Zhang Z, Yang P, Xu H, et al. Surface enhanced fluorescence and Raman scattering by gold nanoparticle dimers and trimers. Journal of Applied Physics. 2013; 113(3). doi: 10.1063/1.4776227
68. Fan X, Zheng W, Singh DJ. Light scattering and surface plasmons on small spherical particles. Light: Science & Applications. 2014; 3(6): e179-e179. doi: 10.1038/lsa.2014.60
69. Nie S, Emory SR. Probing Single Molecules and Single Nanoparticles by Surface-Enhanced Raman Scattering. Science. 1997; 275(5303): 1102-1106. doi: 10.1126/science.275.5303.1102
70. Canovi M, Lucchetti J, Stravalaci M, et al. Applications of Surface Plasmon Resonance (SPR) for the Characterization of Nanoparticles Developed for Biomedical Purposes. Sensors. 2012; 12(12): 16420-16432. doi: 10.3390/s121216420
71. Pyrak E, Jaworska A, Kudelski A. SERS Studies of Adsorption on Gold Surfaces of Mononucleotides with Attached Hexanethiol Moiety: Comparison with Selected Single-Stranded Thiolated DNA Fragments. Molecules. 2019; 24(21): 3921. doi: 10.3390/molecules24213921
72. Lévêque G, Martin OJF. Optical interactions in a plasmonic particle coupled to a metallic film. Optics Express. 2006; 14(21): 9971. doi: 10.1364/oe.14.009971
73. Mock JJ, Hill RT, Degiron A, et al. Distance-Dependent Plasmon Resonant Coupling between a Gold Nanoparticle and Gold Film. Nano Letters. 2008; 8(8): 2245-2252. doi: 10.1021/nl080872f
74. Le Ru EC, Etchegoin PG, Meyer M. Enhancement factor distribution around a single surface-enhanced Raman scattering hot spot and its relation to single molecule detection. The Journal of Chemical Physics. 2006; 125(20). doi: 10.1063/1.2390694

75. Zhang K, Zeng T, Tan X, et al. A facile surface-enhanced Raman scattering (SERS) detection of rhodamine 6G and crystal violet using Au nanoparticle substrates. Applied Surface Science. 2015; 347: 569-573. doi: 10.1016/j.apsusc.2015.04.152
76. Sun S, Wu P. Competitive surface-enhanced Raman scattering effects in noble metal nanoparticle-decorated graphene sheets. Physical Chemistry Chemical Physics. 2011; 13(47): 21116. doi: 10.1039/c1cp22727k
77. Zhang XF, Liu SP, Shao XN. Noncovalent binding of xanthene and phthalocyanine dyes with graphene sheets: The effect of the molecular structure revealed by a photophysical study. Spectrochimica Acta Part A: Molecular and Biomolecular Spectroscopy. 2013; 113: 92-99. doi: 10.1016/j.saa.2013.04.066
78. Dieringer JA, Lettan RB, Scheidt KA, et al. A Frequency Domain Existence Proof of Single-Molecule Surface-Enhanced Raman Spectroscopy. Journal of the American Chemical Society. 2007; 129(51): 16249-16256. doi: 10.1021/ja077243c
79. Zrimsek AB, Chiang N, Mattei M, et al. Single-Molecule Chemistry with Surface- and Tip-Enhanced Raman Spectroscopy. Chemical Reviews. 2016; 117(11): 7583-7613. doi: 10.1021/acs.chemrev.6b00552
80. Marshall ARL, Stokes J, Viscomi FN, et al. Determining molecular orientation via single molecule SERS in a plasmonic nano-gap. Nanoscale. 2017; 9(44): 17415-17421. doi: 10.1039/c7nr05107g
81. Rai VN, Srivastava AK. Correlation between optical and morphological properties of nanostructured gold thin film. JSM Nanotechnology & Nanomedicine. 2016; 4(1).
82. Qin L, Zou S, Xue C, et al. Designing, fabricating, and imaging Raman hot spots. Proceedings of the National Academy of Sciences. 2006; 103(36): 13300-13303. doi: 10.1073/pnas.0605889103
83. Ortega MA, Rodriguez L, Castillo J, et al. Thermo-optical properties of gold nanoparticles in colloidal systems. Journal of Optics A: Pure and Applied Optics. 2008; 10(10): 104024. doi: 10.1088/1464-4258/10/10/104024
84. Seol Y, Carpenter AE, Perkins TT. Gold nanoparticles: enhanced optical trapping and sensitivity coupled with significant heating. Optics Letters. 2006; 31(16): 2429. doi: 10.1364/ol.31.002429
85. Phuoc T, Massoudi M, Wang P. Laser-Induced Motion of a Nanofluid in a Micro-Channel. Fluids. 2016; 1(4): 35. doi: 10.3390/fluids1040035
86. Zhao BS, Koo YM, Chung DS. Separations based on the mechanical forces of light. Analytica Chimica Acta. 2006; 556(1): 97-103. doi: 10.1016/j.aca.2005.06.065
87. Shakib S, Rogez B, Khadir S, et al. Microscale Thermophoresis in Liquids Induced by Plasmonic Heating and Characterized by Phase and Fluorescence Microscopies. The Journal of Physical Chemistry C. 2021; 125(39): 21533-21542. doi: 10.1021/acs.jpcc.1c06299
88. Hrelescu C, Sau TK, Rogach AL, et al. Single gold nanostars enhance Raman scattering. Applied Physics Letters. 2009; 94(15). doi: 10.1063/1.3119642
89. Giannini V, Sánchez-Gil JA. Calculations of light scattering from isolated and interacting metallic nanowires of arbitrary cross section by means of Green's theorem surface integral equations in parametric form. Journal of the Optical Society of America A. 2007; 24(9): 2822. doi: 10.1364/josaa.24.002822
90. Xu H. Theoretical study of coated spherical metallic nanoparticles for single-molecule surface-enhanced spectroscopy. Applied Physics Letters. 2004; 85(24): 5980-5982. doi: 10.1063/1.1833570
91. Yu M, Huang Z, Liu Z, et al. Annealed gold nanoshells with highly-dense hotspots for large-area efficient Raman scattering substrates. Sensors and Actuators B: Chemical. 2018; 262: 845-851. doi: 10.1016/j.snb.2018.02.048
92. Lai CH, Wang GA, Ling TK, et al. Near infrared surface-enhanced Raman scattering based on star-shaped gold/silver nanoparticles and hyperbolic metamaterial. Scientific Reports. 2017; 7(1). doi: 10.1038/s41598-017-05939-0
93. Heinzmann U, Holloway S, Kleyn AW, et al. Orientation in molecule—surface interactions. Journal of Physics: Condensed Matter. 1996; 8(19): 3245-3269. doi: 10.1088/0953-8984/8/19/002
94. Canfield BK, Kujala S, Kauranen M, et al. Remarkable polarization sensitivity of gold nanoparticle arrays. Applied Physics Letters. 2005; 86(18). doi: 10.1063/1.1924886
95. Kim GW, Ha JW. Polarization-Sensitive Single Dipoles Generated from Multiple Sharp Branches on the Surfaces of Single Gold Nanourchins. The Journal of Physical Chemistry C. 2017; 121(36): 19975-19982. doi: 10.1021/acs.jpcc.7b06823